EFFECT OF CENTRIFUGAL FORCE ON THE LOAD CAPACITY OF THRUST GAS BEARING

by

RAKAN MOHAMMEDTAWFIQ I HAIDAR

Presented to the Faculty of the Aerospace & Mechanical Engineering Department of

The University of Texas at Arlington as a partial completion

of the Requirements for the degree of

Master of Science in Mechanical Engineering

THE UNIVERSITY OF TEXAS AT ARLINGTON

December 2022

Acknowledgments

I am wholeheartedly full of profound gratitude to my supervisor, Prof. Daejong Kim for advising, guiding, and encouraging me throughout the last two years led me to achieve the completion of my master's degree thesis, and for giving me the chance to be a team member as well as a graduate research assistant in his turbomachinery lab. I am also fully thankful to my committee members, Profs. Albert Tong, and Bo P Wang for their guidance, and suggestions, as well as for being committee members in my thesis defense. Moreover, I would like to acknowledge all faculty and staff of the MAE department, and all team members working at the turbomachinery lab. Additionally, I stand in recognition to Saudi Government and Taibah University for fully funding me throughout the last two years, which ease me to pay all the tuition fees and expenses and kept me to be fully focused on my studies. I also appreciate the department of Aerospace and Mechanical engineering at the University of Texas at Arlington for granting me the graduate research assistantship in my last semester of studies. Furthermore, I would like to sincerely thank my undergraduate faculty members, especially Prof. Mohamed Abdullatif Aly Omar for encouraging me to pursue my graduate studies, which gave me a huge impulse to know what I am interested in and like to work with. Finally, I would like to greatly thank my parents and siblings for their love and support.

November 21, 2022

Conflict of Interest Disclosure

Dr. Daejong Kim has a potential research conflict of interest (RCOI) due to a financial interest with Bellkim Energy LLC. A RCOI management plan has been placed with The University of Texas at Arlington (UTA) to preserve objectivity in research by UTA policy.

Abstract

EFFECT OF CENTRIFUGAL FORCE ON THE LOAD CAPACITY OF THRUST GAS BEARING

RAKAN M. HAIDAR

The University of Texas at Arlington, 2022

Supervising Professor: Daejong Kim

It has been known for many decades that both rigid and foil thrust bearings are two options in the market for high-speed turbomachinery systems. Their advantages encompass the lower manufacturing cost, the lighter weight, and the flexibility in allowing "component misalignment and runout." When the operating fluid is air, the classical lubrication theory works perfectly. Any additional terms of the inertia effect might be somehow less significant and sometimes negligible since the viscous forces will be dominant, but this may not be the case if the bearing operates in a harsh environment, such as a high-pressure environment. Nonetheless, this is a different scenario when dealing with water or denser gases lubricated bearings since the inertia forces have significance and effects as same as the viscous forces. Therefore, the classical lubrication theory, where the inertia forces are very small – Modified Reynolds number (Re) << 1 – should be rederived and modified to include those additional terms. As they play a major role in affecting the bearing performance by reducing its load capacity, they should be considered. This thesis shows the comparison of both solutions when inertial terms are considered and when they are not through the comparison of the local Reynold number, pressure, streamlines, deflections, and load capacity.

Table of Contents

List of Illustrations

List of Tables

Chapter 1: INTRODUCTION

Thrust Bearing Categorization & Classical Lubrication Theory Entrance

Bearings are the primary structural component of rotating machinery. They come in many types, and they can be categorized based on different criteria, such as the design and working medium, or the direction of the load. The last criterion will be briefly discussed herein. The bearing can be classified based on the direction of loading into radial (Journal) bearings, thrust bearings, and linear bearings. The thrust bearings will be further discussed as this research mainly focuses on the thrust bearings. A thrust bearing can be defined as the main component of a rotating machine that restrains the movement of the shaft along its length. Moreover, the thrust bearings can also be categorized based on the design, such as rolling element thrust bearings, magnetic thrust bearings, and fluid film thrust bearings. The fluid film thrust bearings can also be classified based on the type of lubricant of the bearings, which can be oil, water, or a variety of gases including ambient air. The thrust bearings that operate either by water or gas, oil-free (eco-friendlier to the environment), will be further discussed. Since water and some of the gases have the characteristics of very low viscosity and high molecular weight, respectively when compared to the air, the inertia effects must be considered. Because when lubricants have these characteristics, they can affect the bearings' performance to a great extent. The fluid film thrust bearing can also be classified based on the mode of lubrication as hydrodynamic fluid film bearing or (hydrostatic/hybrid) fluid film bearing. Each mode has a distinctive difference in the operating principle. The hydrodynamic thrust bearing is the bearing "composed of compliant surfaces and generally employs a fluid lubricant," where the runner "drags the viscous fluid into a converging gap," at which the fluid pressure will be increased producing the load-carrying capacity [1]. The hybrid thrust bearing is governed by positive pressure, where it is employed by the lubricant under the pressure between

the stationary and the moving surfaces. The amount of the lubricant being pressurized into the hydrostatic bearing is controlled based on the load on the shaft and the rotational speed. The thrust bearing can also be designed as a rigid bearing, where the bearing's pads are considered rigid (no deflection or perhaps zero deflection). However, the thrust bearing can also be a foil thrust bearing, which is composed of the top foil and the elastic foundation (the corrugated bumps) underneath to be welded to the bearing's backing plate at certain spots. These spots can be determined based on the design. The corrugated bumps provide stiffness and damping to the bearing. Figure 1 illustrates the structure of the hydrodynamic thrust bearing. The hybrid thrust bearing is similar except there are fluid orifices drilled through the two foils through which the lubricant is gushing out from an external source between the stationary surface, the thrust bearing, and the moving surface, the runner. Table 1 shows the main parameters of the gas thrust bearing that will be used throughout this document, and its parameters were used as input to the simulation.

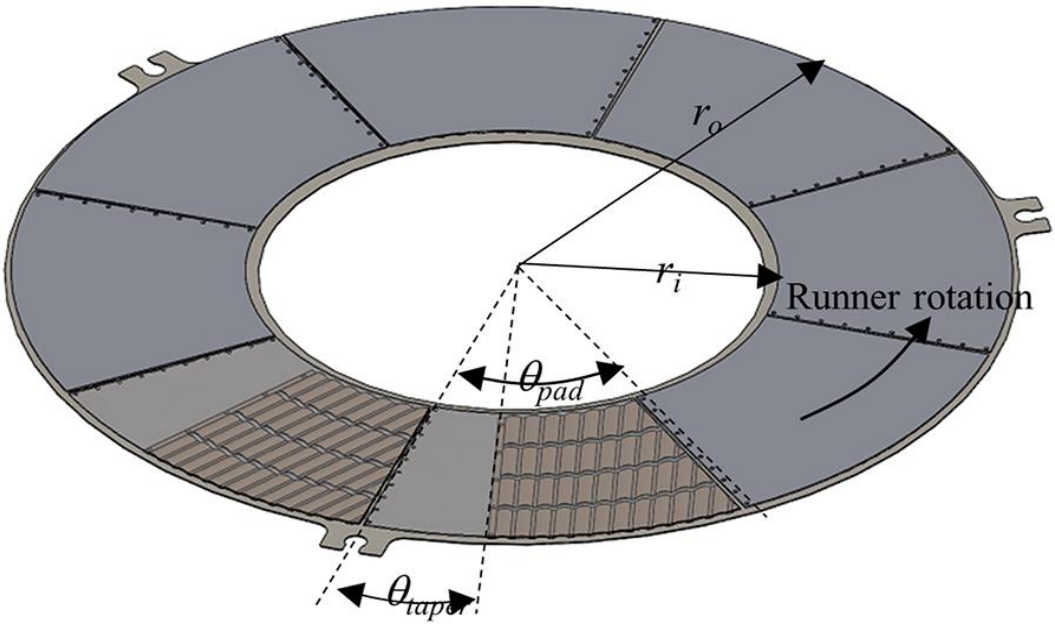

Figure 1: Typical geometry of a hydrodynamic foil thrust bearing, [14]

Table 1: Parameters of gas thrust bearing used in this thesis

Parameters	Value
Inner Radius R_i (mm)	23.5
Outer Radius R_0 (mm)	41.0
Number of Pads	6
Total (Assembly) Clearance, C (μm)	60
Pad Angle	58
Flat to tapered region ratio	0.5
Taper Height (mm)	0.05
Number of Lubricant's Orifices	2
Radial Position of Orifice1 (%) *	0.229
Radial Position of Orifice2 (%) *	0.743
Circuferential Position of Orifice1 (%) *	0.3
Circuferential Position of Orifice2 (%) *	0.3
Radius of Orifices (mm)	0.5
Possible RPM (Current Simulation Speed)	0 – 68000
Total Stiffness of The Corrugated Bumps	200.0e6
Number of Circumferential Grid Points (i), Used in Simulation (n)	120
Number of Radial Grid Points (j), Used in Simulation (m)	60
Temperature (^oC)	250
Young's Modulus Pa	200e9
Poisson Ratio	0.3
External Applied Load	1000 N
Lubricant	Air

* These percentages indicated as the radial position percentages can be multiplied by the radii of (R_o-R_i) to get the radial length at which the two orifices radially located. Similarly, to locate their position circumferentially after getting the radial length from the previous calculation of the lengths associated to the location of the orifices radially, it is possible to multiply those radial lengths by (0.3*Pad Angle) to get the circumferential locations of both orifices. Figure 5 shows the two holes through the bump foil, through which the orifices are being placed within a bearing's pad area.

Chapter 2: LITERATURE REVIEW

There are countless aspects of why bearings' designers may have to include the inertia effects while designing fluid film bearings, such as water or gas-lubricated bearings. First and foremost, some lubricants are much denser than ambient air, such as water, and gases with high molecular weight. Besides, when the bearing operating speed is high. Thus, the classical lubrication theory, where the inertia forces are very small – Modified Reynolds number << 1 – must be modified to consider those additional effects. Second, the centrifugal force can substantially reduce and restrain the bearings' performance, such as the bearings' load capacity. Thirdly, these forces can substantially hinder the lubricant from properly flowing. If one examines the physical properties of the water, and some common gases that are used in fluid film bearings, it is possible to see that the water has very low viscosity compared to conventional lubrication oils, and those common lubricant gases are much denser than the ambient air. Mostly, the common gases used in the fluid film bearings have high molecular weight, which means high density. For a while, these gases have been used for many systems to operate ranging from small compressors to turbine engines. These gases can simultaneously be used to lubricate the gas bearings since these systems can use the same gas to operate. Consequently, knowing how to analyze the performance of the gas bearings is extremely important. For instance, Freon gas (R-134a) can mostly be used in cooling systems as it is the most efficient cooling gas that has ever been known. Therefore, if a turbo compressor, which is usually equipped with gas bearings, is to operate at high speed, it is possible to use R-134a to operate the cycle and lubricate the bearing. Similarly, in the Closed Bryton Cycles (CBC), the supercritical carbon dioxide (sCO2) cycles use carbon dioxide gas that is in a supercritical state, which is another efficient type of gas that can be used for this cycle to operate efficiently.

Comments & Remarks

Inertia effects cannot be neglected when designing fluid film bearings that are lubricated either by water or high-molecular-weight gases, which are highly denser than air, especially when operating at high speed and high Reynold's number, where both inertia effect and turbulence are more pronounced. Even so, sometimes inertia effects should be considered if the lubricant is the air and that is based on taking a high-level precaution because of the high-level precision requirement of the application and the environmental conditions where the bearing is operating. The inertia effect should be considered because it has an effect that can exacerbate the bearing's performance by hindering the proper flow of the lubricant and decreasing the load capacity substantially due to the centrifugal force. From [2], it has been stated because both convective and centrifugal effects are weekly coupled, they can be analyzed and tested separately. The centrifugal effect has a negative effect by reducing the load capacity while the convective effect has a positive effect by increasing the load-carrying capacity. Furthermore, in the case of the tilting pad thrust bearing, when the film thickness ratio is small or the extent angle is large, the centrifugal effect is the highest in the medium, and that will cause a reduction in the load-carrying capacity. Nonetheless, when the film thickness ratio is large, or the extent angle is small, the convective effect is dominant, and that will cause an increase in the load-carrying capacity. Noteworthy, both centrifugal and convective forces are canceling each other at which both the film thickness ratio and the extent angle are moderate. From [3], it has been shown that the ratio of the radii has a pronounced influence on the load capacity, where it decreases when the inertia effect is considered compared to the inertia-less case. As previously mentioned, the highly dense gases presented in Table 2 can be used as a working fluid as well as a lubricant for the hydrostatic bearings in the mechanical closed cycles to operate, such as Closed Bryton Cycles (CBC) that operate using

supercritical carbon dioxide (sCO2). From [13], using supercritical carbon dioxide in a Closed Bryton Cycle would be a brilliant idea for many reasons. First, due to its high density and volumetric heat capacity, that will help reduce the size of the cycle when compared to the conventional cycle size which would require less budget and cost. Second, it is considered an ideal working fluid because it is non-explosive, non-flammable, and non-toxic. Lastly, it is relatively cheap compared to other working fluids. Therefore, the advantages of the hydrostatic foil bearings greatly outweigh the advantages of the oil-lubricated bearings if used in closed systems that operate with gases. From [6], some gases have been tested in the High-Pressure Rig at *NASA Glenn Research Center* to monitor the bearing's power loss; it has been found that the bearing's power loss greatly depends on the gas density and the shaft speed. There is a threshold speed above which the bearing's power loss increases with the increase of the pressure, and the threshold speed increases as the gas molecular weight decreases. Thus, the inertia forces play a major role in affecting the bearing's power loss. From another perspective, when testing and analyzing the bearing performance, one of the important matters that can be analyzed and tested is the bearing's stability. From [7], it has been recommended that the inertia effect must be considered when the modified Reynold number is greater than one because those terms can drastically deteriorate the bearings' performance. This is true, and it has been verified how those terms can affect the thrust bearing's performance, such as the bearings' load capacity. However, they concluded that those inertia terms could enhance the journal bearings' performance by increasing the bearings' stability. Their conclusion opposes the conclusion of this current work because centrifugal force is detrimentally worsening the thrust bearing's load-carrying capacity. Also, this might be different for the case of journal bearing. Therefore, this issue should be addressed further. From [8], it has been concluded that in some situations even though the flow of the lubricants is laminar, the inertia

effects can play a major role and cannot be neglected because of the high velocity of the lubricants as they have a low viscosity, such as synthetic lubricants. Therefore, the stability of the rotor kept worsening even at a lower eccentricity ratio with the increase of the ratio of the bearing's length to its diameter (L/D).

Table 2:Viscosity & molecular weight of gases used in thin-film bearings [4]

Gas	**Chemical Formula**	**Molecular weight (g/mol)**	**μ_o μPa-s**	**T^o K**	**T* K**
Acetylene	C_2H_2	26.036	10.2	293	198
Air	O_2+N	29.000	17.1	273	124
Ammonia	NH_3	17.034	9.82	293	626
Argon	Ar	39.950	22.04	289	143
Carbon Dioxide	CO_2	44.010	13.66	273	274
Carbon Monoxide	CO	28.010	16.65	273	101
Chlorine	Cl_2	70.900	12.94	289	351
Chloride	HCL	36.458	13.32	273	360
Helium	He	4.003	18.6	273	38
Hydrogen	H_2	2.016	8.5	273	83
Hydrogen sulfide	H_2S	34.086	12.51	290	331
Methane	CH_4	16.042	10.94	290	198
Neon	Ne	20.180	29.73	273	56
Nitrogen	N_2	28.020	16.65	273	103
Nitric Oxide	NO	30.010	17.97	273	162
Nitrous Oxide	N_2O	44.020	13.66	273	274
Oxygen	O_2	32.000	19.2	273	138
Steam	H_2O	18.016	12.55	372	673
Sulfur Dioxide	SO_2	64.070	11.68	273	416
Xenon	Xe	131.300	21.01	273	220
Gas constant R = (8,314,34 J/Kg-K)/MW					

Chapter 3: DERIVATION, MODIFICATION, CODING, AND SIMULATION

Classical Lubrication Theory

The Classical Lubrication Equation or perhaps the so-called Classical Reynolds Equation is the equation "based on the work of Osborne Reynolds (Reynolds, 1886)." which gave birth to the science of hydrodynamic lubrication," (Khonsari 2017) [9]. The Classical Reynolds Equation is based on the assumptions of negligible flow inertia and curvature effect due to the low Reynolds number and the thin film, respectively. Similarly, the Classical Reynold Equation in polar coordinates can be derived as the Classical Reynold Equation in the cartesian coordinate, or it can be obtained through the coordinate transformation from cartesian to polar coordinates. The classical Reynolds equation in polar coordinates is given by the equation(1).

$$\frac{1}{R}\frac{\partial}{\partial r}\left(R\frac{\rho h^3}{12\mu}\frac{\partial p}{\partial r}\right)+\frac{1}{R}\frac{\partial}{\partial \theta}\left(\frac{\rho h^3}{12\mu}\frac{\partial p}{R\partial \theta}\right)=\frac{R\omega}{2}\frac{\partial(\rho h)}{R\partial \theta}+\frac{\partial(\rho h)}{\partial t} \tag{1}$$

Where, $\partial/\partial r$ is the partial derivative concerning the radial direction (r) or (η);(r) indicates the dimensional coordinate while (η) indicates the nondimensional coordinate. $\partial/\partial\theta$ is the partial derivative concerning the circumferential direction (θ), (p) is the pressure, (R) is the radius, (ω) is the angular velocity, (ρ) is the density, (μ) is the dynamic viscosity, (t) is the time, and (h) is the film thickness, which is illustrated in Figure 2 and defined by equations(2) and(3).

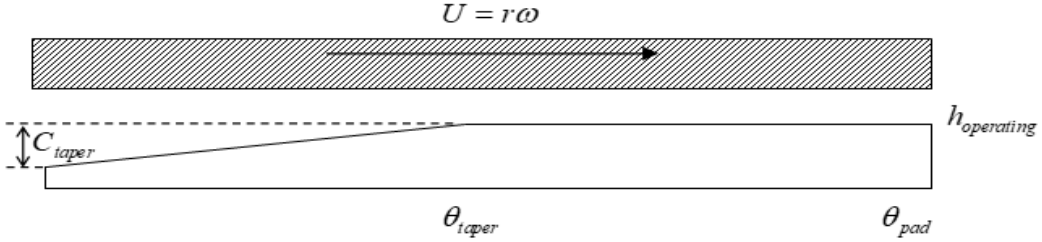

Figure 2: Cross-sectional configuration of the thrust bearing [9]

$$h_{operating} = C_T - z_{runner} \tag{2}$$

, where C_T is the assembly clearance z_{runner} is the axial displacement

$$\begin{aligned} h &= h_{operating} + C_{taper}\left(1 - \frac{\theta}{\theta_{taper}}\right) \quad 0 < \theta < \theta_{taper} \\ h &= h_{operating} \quad \theta_{taper} < \theta < \theta_{pad} \end{aligned} \tag{3}$$

Modified Reynolds Equation with Inertia Effects

When including those terms associated with the inertia effects, the classical Reynolds Equation in polar coordinates will be modified, and it can be called the modified Reynolds equation. This equation is fully discussed and derived by Pinkus and Lund in reference [8], and this derivation procedure will be discussed again in this document. To derive this Equation, the assumption of constant property across the film has been made. As it has been done to derive the Classical Reynold Equation, this derivation starts from continuity and momentum equations. However, the resulting Navier-Stocks equations that should be taken into consideration after imposing the continuity equation into the momentum equations will be a bit different and complicated. Both Navier-Stocks equations when deriving the classical Reynolds equation and the Modified Reynolds equation differ because the terms on the left-hand side of the Navier-Stocks equations are to be considered when deriving the modified Reynolds equation. Those terms are to be included when considering the inertia effects since the modified Reynolds' number may be higher or equal to 1. Nevertheless, the third equation of the Navier-Stocks equations representing the lubricant flow along the axial axis (*w*) will be neglected because of the " usual assumptions in lubrication theory about the smallness of *w*, ($\partial p / \partial y$), etc," (Pinkus and Lund 1981) [8], knowing that *w* represents the velocity vector of the lubricant in the direction out of the paper. Noteworthy, the reference of all the derivations in this section follows Pinkus and Lund. Therefore, the Navier-

Stocks Equations for the sectorial configuration illustrated in Figure 3 will be given by equations(4) and(5).

$$v\left(\frac{\partial u}{\partial r}\right)+\frac{u}{r}\left(\frac{\partial u}{\partial \theta}\right)+\frac{uv}{r}=-\frac{1}{\rho r}p_{\theta}+\frac{\mu}{\rho}\left(\frac{\partial^2 u}{\partial y^2}\right) \tag{4}$$

$$v\left(\frac{\partial v}{\partial r}\right)+\frac{u}{r}\left(\frac{\partial v}{\partial \theta}\right)-\left(\frac{u^2}{r}\right)=-\frac{1}{\rho}p_{r}+\frac{\mu}{\rho}\left(\frac{\partial^2 v}{\partial y^2}\right) \tag{5}$$

Now, as the runner is rotating relative to the stationary surface, the bearing surface, equations(6) and(7) can be formed. The subscript of s indicates the shear-induced flow, and the subscript of p indicates the pressure gradient.

$$u=u_s+u_p \tag{6}$$

$$v=v_p \tag{7}$$

Pinkus and Lund stated, “in most bearing applications, particularly for bearings with high linear speed, we will have,” the following assumption.

$$u_p << u_s \quad , \quad v \equiv v_p << u_s$$

Now, both equations(4) and(5) can be written as equations(8) and(9) when aiming to evaluate the inertia forces.

$$\frac{1}{r}p_{\theta}=\mu\left(\frac{\partial^2 u}{\partial y^2}\right)-\frac{\rho u_s}{r}\cdot\left(\frac{\partial u_s}{\partial \theta}\right) \tag{8}$$

$$p_r=\mu\left(\frac{\partial^2 v}{\partial y^2}\right)+\frac{\rho u_s}{r}\cdot u_s \tag{9}$$

Then, it has been assumed since $u_s = U(y/h)$, the value of u_s will be the same at any location of angular position (θ). Therefore, the following expression in the equation(10) holds, and the term left is the centrifugal term only.

$$\left(\frac{\partial u_s}{\partial \theta}\right) \simeq 0 \tag{10}$$

Consequently, equations(8) and(9) can also be written as equations(11) and(12).

$$\mu \frac{\partial^2 u}{\partial y^2} = \frac{1}{r} p_\theta \tag{11}$$

$$\mu \frac{\partial^2 v}{\partial y^2} = p_r - \left(\frac{\rho u^2}{r}\right) \tag{12}$$

Now, it is possible to integrate both equations(11) and(12) over the film thickness with the consideration of the following boundary conditions. After integrating, both velocities distribution of *u* and *v* are given by equations(13) and(14) , respectively, following the Pinkus and Lund paper, [8].

$$u = r\omega \quad , \; v = 0 \text{ at } y = 0$$
$$u = 0 \quad , \; v = 0 \text{ at } y = h$$

$$u = \left[\omega(h-y) + \omega_B y\right]\frac{r}{h} - \frac{y(h-y)}{2\mu r} p_\theta \tag{13}$$

$$v = \frac{\left(\rho r\omega^2 - p_r\right)}{2\mu} y(h-y) + \frac{\rho y}{\mu r}\left[K_1\left(h^2 - y^2\right) + K_2\left(h^3 - y^3\right) + K_3\left(h^4 - y^4\right) + K_4\left(h^5 - y^5\right)\right] \tag{14}$$

, where

$$K_1 = -\left[\frac{h^2}{2\mu}\, p_\theta + r^2\left(\omega - \omega_B\right)\right]\frac{\omega}{3h}$$

$$K_2 = \frac{1}{12}\left\{\left[\frac{r\left(\omega-\omega_B\right)}{h}\right]^2 + \frac{1}{2\mu}\, p_\theta\left[\frac{1}{2\mu}\left(\frac{h}{r}\right)^2 p_\theta + 2\left(2\omega - \omega_B\right)\right]\right\}$$

$$K_3 = -\frac{1}{20\mu}\, p_\theta\left[\frac{h}{2\mu r^2}\, p_\theta + \frac{\left(\omega-\omega_B\right)}{h}\right]$$

$$K_4 = \frac{1}{30}\left(\frac{1}{2\mu r}\, p_\theta\right)^2$$

$$p_\theta = \frac{\partial p}{\partial \theta} \qquad p_r = \frac{\partial p}{\partial r}$$

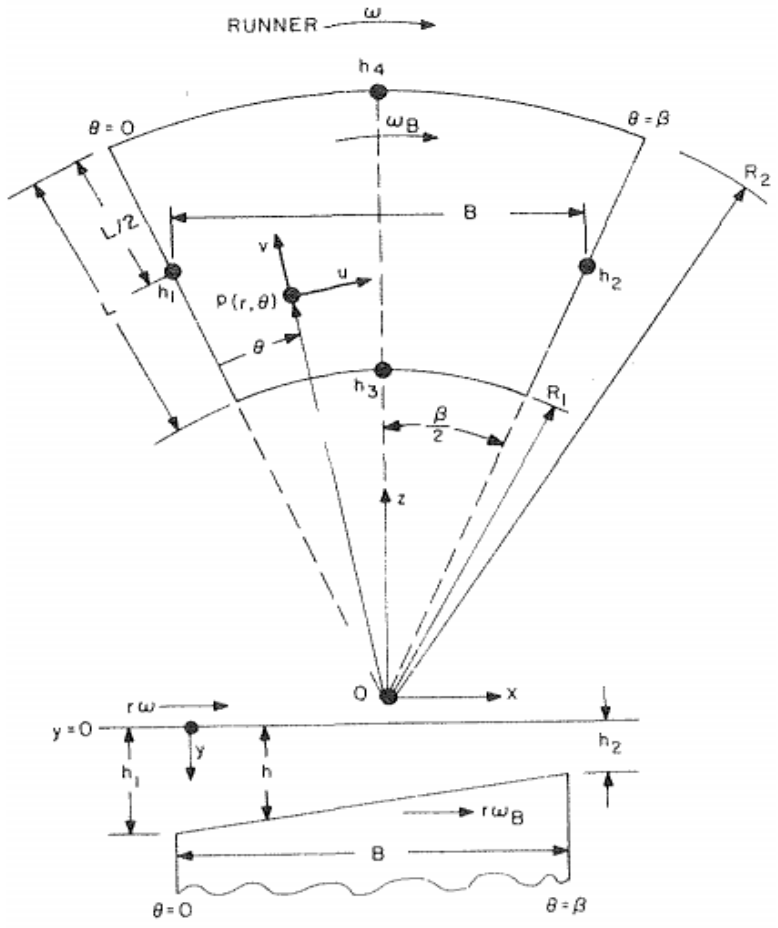

Figure 3: Basic nomenclature of bearing's sectorial configuration [8]

After obtaining both equations(13) and(14), it is possible to do the dynamic balance over the control volume of the sectorial configuration shown in Figure 3. The control volume of the bearing's sectorial configuration is illustrated in Figure 4.

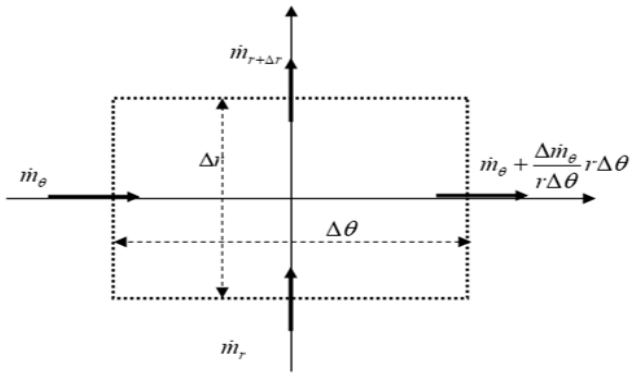

Figure 4: Control volume of the bearing sectorial configuration [10]

After doing the dynamic balance, the obtained equation will be given by the equation(15). After substituting all parameters, Ks' values are defined in equation(14), rearranging, changing the derivatives to a partial derivative form, and multiplying the whole equation by -1, equation(15) can be rewritten and represented by equation(16).

$$\Delta\dot{m}_\theta + \dot{m}_{r+\Delta r} - \dot{m}_r + \frac{\Delta}{\Delta t}\left(m_{CV}\right) = 0 \tag{15}$$

, where

$$\dot{m}_\theta = \int_0^h \left(\rho \Delta r u(\theta)\right) dy = q_\theta \Delta r$$

$$\dot{m}_r = \int_0^h \rho r \Delta\theta v(r) dy = q_r r \Delta\theta$$

$$\dot{m}_{r+\Delta r} = \int_0^h \rho\left(r+\Delta r\right)\Delta\theta v\left(r+\Delta r\right) dy = \left(q_r + \frac{\partial q_r}{\partial r}\Delta r\right)\left(r+\Delta r\right)\Delta\theta$$

$$q_r = \left(-\frac{\rho h^3}{12\mu}\frac{\partial p}{\partial r} + \frac{\rho^2 r\omega^2 h^3}{12\mu} + \frac{\rho^2}{\mu r}\left[K_1\left(\frac{h^4}{4}\right) + K_2\left(\frac{3h^5}{10}\right) + K_3\left(\frac{h^6}{3}\right) + K_4\left(\frac{5h^4}{14}\right)\right]\right)$$

$$q_\theta = -\frac{\rho h^3}{12\mu}\frac{\partial p}{r\partial\theta} + \frac{\rho\omega h r}{2} \qquad m_{CV} = \rho h r \Delta\theta \Delta r$$

$$\frac{\partial}{r\partial\theta}\left(\frac{\rho h^3}{12\mu}\frac{\partial p}{r\partial\theta}-\frac{\rho\omega hr}{2}\right)+\frac{\partial}{r\partial r}\left(\frac{\rho r h^3}{12\mu}\frac{\partial p}{\partial r}-\frac{3\rho^2 r^2\omega^2 h^3}{120\mu}\right)=\frac{\partial}{\partial t}(\rho h)$$
$$-\frac{1}{120}\frac{\partial}{r\partial r}\left(\frac{\rho^2 r h^5}{\mu^3}\frac{\partial p}{r\partial\theta}\left(\mu\omega-\frac{3h^2}{28r}\frac{\partial p}{r\partial\theta}\right)\right) \tag{16}$$

This is generally the modified Reynold's equation including inertia force in convection-diffusion form. For gases, density in equation(16) can be replaced with pressure using the equation of state, equation(17).

$$\rho=\frac{p}{R_g T} \tag{17}$$

Thus, equation(16) can be represented by equation(18).

$$\frac{\partial}{r\partial\theta}\left(\frac{h^3 p}{12\mu R_g T}\frac{\partial p}{r\partial\theta}-\frac{\omega hrp}{2R_g T}\right)+\frac{\partial}{r\partial r}\left(\frac{rh^3 p}{12\mu R_g T}\frac{\partial p}{\partial r}-\frac{3\rho r^2\omega^2 h^3 p}{120\mu R_g T}\right)=\frac{\partial}{\partial t}\left(\frac{hp}{R_g T}\right)$$
$$-\frac{1}{120}\frac{\partial}{r\partial r}\left(\frac{\rho r h^5 p}{\mu^3 R_g T}\frac{\partial p}{r\partial\theta}\left(\mu\omega-\frac{3h^2}{28r}\frac{\partial p}{r\partial\theta}\right)\right) \tag{18}$$

For the isothermal case, $R_g T$ can be dropped off of the whole equation and if multiplying both sides of the equation by 12 so that equation(18) can also be expressed by equation(19).

$$\frac{\partial}{\partial\theta}\left(\frac{h^3 p}{\mu}\frac{\partial p}{r\partial\theta}-6\omega hrp\right)+\frac{\partial}{\partial r}\left(\frac{rh^3 p}{\mu}\frac{\partial p}{\partial r}-\frac{3\rho r^2\omega^2 h^3 p}{10\mu}\right)=12\frac{\partial}{\partial t}(rhp)$$
$$-\frac{1}{10}\frac{\partial}{\partial r}\left(\frac{\rho r h^5 p}{\mu^3}\frac{\partial p}{r\partial\theta}\left(\mu\omega-\frac{3h^2}{28r}\frac{\partial p}{r\partial\theta}\right)\right) \tag{19}$$

Equation(19) is the modified Reynolds equation for compressible gases including centrifugal inertia force. When inertia is all neglected, equation(19) is reduced to the traditional thin film Reynolds equation, equation(20).

$$\frac{\partial}{\partial\theta}\left(\frac{h^3 p}{\mu}\frac{\partial p}{r\partial\theta}-6\omega hrp\right)+\frac{\partial}{\partial r}\left(\frac{rh^3 p}{\mu}\frac{\partial p}{\partial r}\right)=12\frac{\partial}{\partial t}(rhp) \tag{20}$$

Non-dimensional Modified Reynolds Equation

It is also possible to represent equation(19) in a non-dimensional form using the following nondimensional parameters.

$$P=\frac{pC_T^2}{\mu U_T R_T};\eta=r/R_T;Z=z/C_T;V_\theta=\frac{v_\theta}{U_T};V_Z=\frac{R_T}{C_T}\frac{v_z}{U_T};V_r=\frac{v_r}{U_T};\tau=\omega t;\bar{\mu}=\frac{\mu}{\mu_0(T_0)}$$

, where $U_T=R_T\omega=(R_i+R_o)\omega/2$ P_a=101325 Pa

Now, equation(19) can be expressed by equation(21).

$$\begin{aligned}&\frac{\partial}{\partial\theta}\left(\Lambda_0\eta HP-\frac{1}{\eta}\frac{PH^3}{\bar{\mu}}\frac{\partial P}{\partial\theta}\right)+\frac{\partial}{\partial\eta}\left(\frac{\mathrm{Re}'\Lambda_0}{20}\frac{\eta^2H^3}{\bar{\mu}}P-\eta\frac{PH^3}{\bar{\mu}}\frac{\partial P}{\partial\eta}\right)=-2\frac{\partial}{\partial\tau}(\eta HP)\\&+\frac{1}{10}\frac{\partial}{\partial\eta}\left(\frac{\mathrm{Re}'\eta PH^5}{\bar{\mu}^3}\frac{\partial P}{\eta\partial\theta}\left(\bar{\mu}-\frac{9}{\Lambda_0 14}\frac{H^2}{\eta}\frac{\partial P}{\eta\partial\theta}\right)\right)\end{aligned} \tag{21}$$

, where

$$\Lambda_0=\frac{6\mu\omega}{p_a}\left(\frac{R_i}{C_T}\right)^2 \qquad \mathrm{Re}'=\frac{\omega\rho R_i^{\,2}}{\mu_0}\left(\frac{C}{R_i}\right)^2$$

Equation(21) can also be condensed to be represented by equation(22) .

$$\frac{\partial\dot{Q}_\theta}{\partial\theta}+\frac{\partial\dot{Q}_\eta}{\partial\eta}=-Q_s \tag{22}$$

, where

$$\dot{Q}_\theta = \Lambda_0 \eta HP - \frac{1}{\eta}\frac{PH^3}{\bar{\mu}}\frac{\partial P}{\partial \theta} \tag{23}$$

$$\dot{Q}_\eta = \frac{\mathrm{Re}'\Lambda_0}{20}\frac{\eta^2 H^3}{\bar{\mu}}P - \eta\frac{PH^3}{\bar{\mu}}\frac{\partial P}{\partial \eta} \tag{24}$$

$$Q_s = 2\frac{\partial}{\partial \tau}(\eta HP) - \frac{1}{10}\frac{\partial}{\partial \eta}\left(\frac{\mathrm{Re}'\eta PH^5}{\bar{\mu}^3}\frac{\partial P}{\eta \partial \theta}\left(\bar{\mu} - \frac{9}{\Lambda_0 14}\frac{H^2}{\eta}\frac{\partial P}{\eta \partial \theta}\right)\right) \tag{25}$$

The first term in equation(23) is the shear-driven term, and the second term is pressure-driven along the circumferential direction. The first term in equation(24) is the centrifugal force, and the second term is pressure-driven along the radial direction. Q_s indicates the flux term of the right-hand side term of equation(19); it is given by equation(25). The first term is the transient term, and the second term is the new term associated with the inertia effect.

Coding and Simulation of Modified Reynolds Equation

The main objective of this thesis is to derive and add the inertia effects to the classical lubrication equation. Not only this but also to solve the classical Reynolds equation as well as the modified Reynolds equation to compare the solutions and investigate how those inertia terms affect the thrust bearing's performance or perhaps the bearing's load capacity. The first step was to implement those new terms in the classical Reynolds equation solver. The thrust foil bearing code has the capability and a wide variety of options, it can simulate both the rigid as well as the foil bearing. It also has the option to simulate both solutions while including the inertia terms and while not. Further. It also has the option to solve Reynold's equation only once for the case of the rigid bearing while giving the minimum film thickness as an input, and then a comparison can be done between the two solutions to investigate the difference in pressure and the bearing's load capacity. However, this method cannot be used when solving the case of the foil gas bearing because of the deflection that occurs to the bearing's foils with time. Therefore, the transient method is rather be

used to solve for the gas foil bearing. Consequently, Reynold's equation is solved iteratively by the Gauss-Seidel at each nodal point of a bearing's pad, where it keeps iterating until mapping out the steady-state solution. When simulating the foil gas bearing, there is an elastic foundation (the corrugated bumps) that provides both bearing's stiffness and damping coefficients. The bumps foil can be visualized to be welded to the bearing's backing plate, usually almost halfway from the leading edge, and on top of that, the top foil is welded to the bearing's backing plate at the leading edge of the bearing's pad as it is clearly illustrated in Figure 1. "Once the pressure profile is evaluated, all other bearing performance such as load-carrying capacity, friction force, flow rate, etc., can easily be determined," (Khonsari 2017) [9]. Therefore, it is possible to plot the pressure profile from the numerical data. The bump mapping is critically needed to run this code for the gas foil bearing mode. It needs the bump mapping numerical data where the elastic foundation and the corrugated bumps are touching the backing plate. These numerical data are needed as input to the bump deflection subroutine function to calculate the deflection of the bearing's foils. This bump deflection subroutine function is modeled as a 2D plate model. The input file can be generated using a simple code written in MATLAB. This code can generate the required bump mapping file if the dimensions of the radial slots are predicted and implemented in the MATLAB code. Basically, the bump mapping file is numerical data, which are represented by zeros & ones, where the zeros mean the corrugated bumps are not touching the bearing's backing plate, yet the ones mean touching. Figure 5 shows the Solid Works (CAD) Model of the actual bearing's corrugated bumps foil.

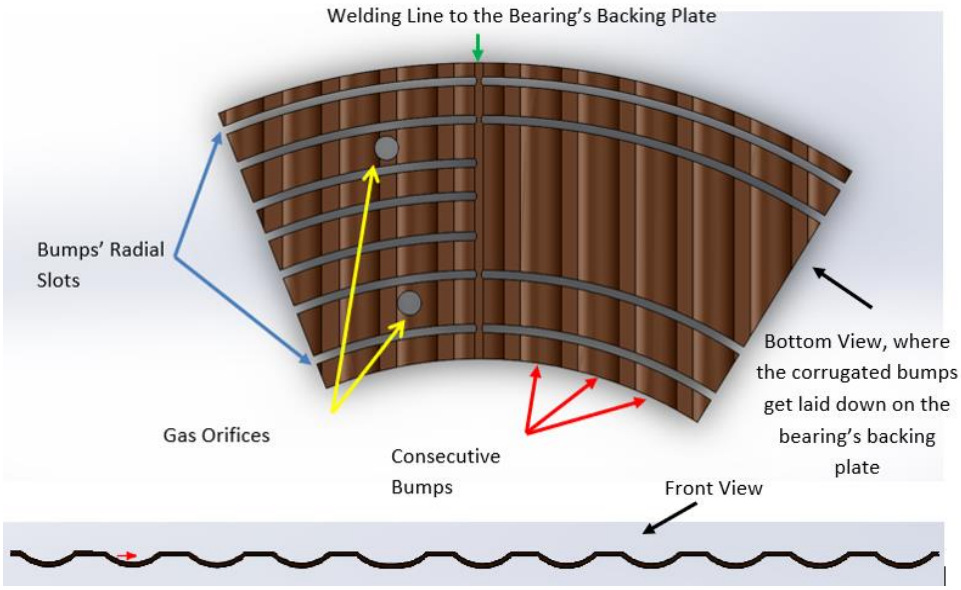

Figure 5: Bottom & front views of the actual corrugated bumps

Figure 6 shows the bearing's bumps mapping configuration of the bearing's six pads, where the yellow lines represent the values of ones of the numerical date in the mapping input file, and the blue areas enclosed by those yellow lines, are the areas of the zeros' numerical values.

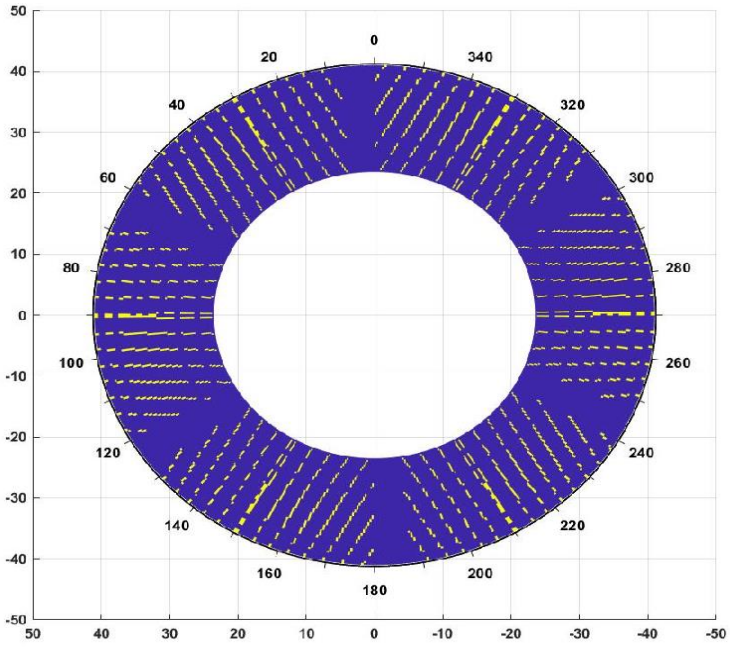

Figure 6: Polar plot of the corrugated bumps of the six pads

Discretization of Modified Reynolds Equation

To introduce equation(22) to the code, it should be in a discretized form; the method of the discretization can be fully found in the book of Numerical Heat Transfer and Fluid Flow, (Patankar 1980), [10]. After the discretization, it is possible to apply the method of undetermined coefficients, which is also widely known as the finite element difference scheme (forward, backward, and central difference), which are applied to the right-hand side term, the source term Q_s, of the Modified Reynolds Equation, equation(25). The forward scheme of the first order is given by equation (26) while the backward scheme is given by equation (27).

$$\left.\frac{\partial w}{\partial x}\right|_{+} \cong \frac{-3w(x)+4w(x+h)-w(x+2h)}{2h} \tag{26}$$

$$\left.\frac{\partial w}{\partial x}\right|_{-} \cong \frac{+3w(x)-4w(x-h)+w(x-2h)}{2h} \tag{27}$$

Equation (28) gives the mathematical expression for the central difference scheme. *h* is the distance between two consecutive grid points.

$$\left.\frac{\partial w}{\partial x}\right| \cong \frac{w(x+h)-w(x-h)}{2\Delta h} \tag{28}$$

If one looks at Figure 7, it is easily can be seen that the yellow grid point is the current grid point, and the blue grid points are the points halfway from the current grid points and are the intended points to be calculated at this instance while the red grid points are a single grid point away from the current grid point. Those forward and backward difference schemes are applied on the boundaries of the control volume represented by

Figure 4 mainly on the source term, Q_s, but the central difference scheme is applied everywhere on the area enclosed by the boundaries of the four sides. This method is mainly applied to make sure that the code is reading the numerical data enclosed by the pressure control volume as illustrated in Figure 7. Going beyond this control volume when reading the numerical data of the source term, the results will not converge. Consequently, the forward scheme is needed at the south and west sides while the backward is needed at the north as well as the east side.

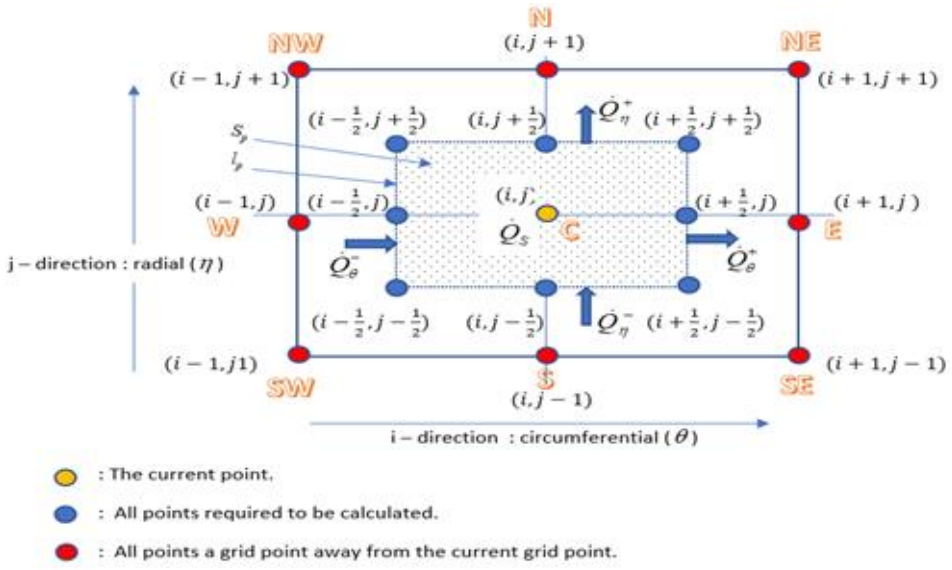

Figure 7: Bearing's control volume of a single grid point of a single pad

If expressing equation(22) in incremental form, it can be rewritten by equation(29). This equation is the Modified Reynolds Equation in flux form.

$$\dot{Q}_\theta^+ - \dot{Q}_\theta^- + \dot{Q}_\eta^+ - \dot{Q}_\eta^- = Q_s \tag{29}$$

The first term of equation(29) is the flux term along the circumferential direction of the positive increment, which is given by equation(30). Equation(30) also represents this term in a discretized form of a convection-diffusion term.

$$\dot{Q}_{\theta}^{+}=\left(\eta\Lambda HP-\frac{1}{\eta}PH^{3}\frac{\partial P}{\partial\theta}\right)_{i+1/2,j}\Delta\eta=\left(\frac{F_{i+1/2,j}}{2}-D_{i+1/2,j}^{\theta}\right)P_{i+1,j}+\left(\frac{F_{i+1/2,j}}{2}+D_{i+1/2,j}^{\theta}\right)P_{i,j} \quad (30)$$

, where $F_{i+\frac{1}{2},j}^{\theta}=\Lambda H_{i+\frac{1}{2},j}\eta_{i+\frac{1}{2},j}\Delta\eta \qquad D_{i+\frac{1}{2},j}^{\theta}=\left(\frac{PH^{3}}{\eta}\right)_{i+\frac{1}{2},j}\frac{\Delta\eta}{\Delta\theta}$

Similarly, the second term of equation(29) is the flux term along the circumferential direction of the negative increment. This term is given by equation(31); equation(31) also represents this term in a discretized form of a convection-diffusion term.

$$\dot{Q}_{\theta}^{-}=\left(\eta\Lambda HP-\frac{1}{\eta}PH^{3}\frac{\partial P}{\partial\theta}\right)_{i-1/2,j}\Delta\eta=\left(\frac{F_{i-1/2,j}}{2}-D_{i-1/2,j}^{\theta}\right)P_{i-1,j}+\left(\frac{F_{i-1/2,j}}{2}+D_{i-1/2,j}^{\theta}\right)P_{i,j} \quad (31)$$

, where $F_{i-\frac{1}{2},j}^{\theta}=\Lambda H_{i-\frac{1}{2},j}\eta_{i-\frac{1}{2},j}\Delta\eta \qquad D_{i-\frac{1}{2},j}^{\theta}=\left(\frac{PH^{3}}{\eta}\right)_{i-\frac{1}{2},j}\frac{\Delta\eta}{\Delta\theta}$

Likely, the third term of equation(29) is the flux term along the radial direction of the positive increment. This term is given by equation(32); this term is also represented in a convection-diffusion term.

$$\begin{aligned}\dot{Q}_{\eta}^{+}&=\left(\left(\frac{\mathrm{Re}'_{0}}{20}\eta^{2}PH^{2}\right)\Lambda HP-\eta PH^{3}\frac{\partial P}{\partial\eta}\right)_{(i,j+1/2)}\Delta\theta\\&=-\left(D_{(i,j+1/2)}^{\eta}-\frac{F_{(i,j+1/2)}^{\eta}}{2}\right)P_{(i,j+1)}+\left(\frac{F_{(i,j+1/2)}^{\eta}}{2}+D_{(i,j+1/2)}^{\eta}\right)P_{(i,j)}\end{aligned} \quad (32)$$

, where $F_{(i,j+1/2)}^{\eta}=\left(\frac{\mathrm{Re}_{0}^{'}}{20}\Lambda\eta^{2}PH^{3}\Delta\theta\right)_{(i,j+1/2)} \qquad D_{(i,j+1/2)}^{\eta}=\left(\eta PH^{3}\frac{\Delta\theta}{\Delta\eta}\right)_{(i,j+1/2)}$

$$\bar{\rho}=\frac{\rho}{\rho_{0}} \qquad \bar{\mu}=\frac{\mu}{\mu_{0}} \qquad \bar{\rho}=\frac{\rho}{\rho_{0}}=\frac{p/RT_{a}}{p_{a}/RT_{a}}=\frac{p}{p_{a}}=P$$

$$\mathrm{Re}' = \frac{\omega\rho R_i^{\,2}}{\mu_0}\left(\frac{C}{R_i}\right)^2 = \frac{\omega\rho_0 R_i^{\,2}}{\mu_0}\left(\frac{C}{R_i}\right)^2 \bar{\rho} = \mathrm{Re}_0' P$$

Similarly, the Fourth term of equation(29) is the flux term along the radial direction of the negative increment. This term is given by equation(33). This term is also expressed in a convection-diffusion term.

$$\begin{aligned}\dot{Q}_\eta^- &= \left(\left(\frac{\mathrm{Re}'_0}{20}\eta^2 PH^2\right)\Lambda HP - \eta PH^3\frac{\partial P}{\partial \eta}\right)_{(i,j-1/2)}\Delta\theta \\ &= -\left(D^\eta_{(i,j-1/2)} - \frac{F^\eta_{(i,j-1/2)}}{2}\right)P_{(i,j)} + \left(\frac{F^\eta_{(i,j-1/2)}}{2} + D^\eta_{(i,j-1/2)}\right)P_{(i,j-1)}\end{aligned} \tag{33}$$

, where $F^\eta_{(i,j-1/2)} = \left(\frac{\mathrm{Re}'_0}{20}\Lambda\eta^2 PH^3\Delta\theta\right)_{(i,j-1/2)}$ $D^\eta_{(i,j-1/2)} = \left(\eta PH^3\frac{\Delta\theta}{\Delta\eta}\right)_{(i,j-1/2)}$

$$\mathrm{Re}' = \frac{\omega\rho R_i^{\,2}}{\mu_0}\left(\frac{C}{R_i}\right)^2 = \frac{\omega\rho_0 R_i^{\,2}}{\mu_0}\left(\frac{C}{R_i}\right)^2 \bar{\rho} = \mathrm{Re}_0' P$$

Lastly, the fifth, or perhaps the right-hand term of equation(29) is the source term and is given by equation(34). the first term of this equation, (the squeeze term) will be equal to zero when solving for the steady-state case but not when solving for the unsteady state (the transient method). The second term, which is associated with the inertia terms, can be separately represented by equation(35).

$$Q_s = 2\Lambda_0\frac{\Delta\theta\Delta\eta}{\Delta\tau}\left(\eta PH\right) - \frac{1}{10}\frac{\partial}{\partial\eta}\left(\mathrm{Re}'\frac{\eta PH^5}{\bar{\mu}^3}\frac{\partial P}{\eta\partial\theta}\left(\bar{\mu} - \frac{9}{14\Lambda_0}\frac{H^2}{\eta}\frac{\partial P}{\eta\partial\theta}\right)\right)\Delta\theta\Delta\eta \tag{34}$$

$$Q_{ss} = -\frac{1}{10}\frac{\partial}{\partial\eta}\left(\mathrm{Re}'\frac{\eta PH^5}{\bar{\mu}^3}\frac{\partial P}{\eta\partial\theta}\left(\bar{\mu} - \frac{9}{14\Lambda_0}\frac{H^2}{\eta}\frac{\partial P}{\eta\partial\theta}\right)\right)\Delta\theta\Delta\eta \tag{35}$$

, where $\Lambda_0 = \frac{6\mu_0\omega}{p_a}\left(\frac{R_i}{C}\right)^2$ $\mathrm{Re}' = \frac{\omega\rho R_i^2}{\mu_0}\left(\frac{C}{R_i}\right)^2 = \frac{\omega\rho_0 R_i^2}{\mu_0}\left(\frac{C}{R_i}\right)^2 \bar{\rho} = \mathrm{Re}_0' P$

Considering a special case for isothermal case, where $\bar{\mu} = 1$, equation(35) will be reduced to equation(36).

$$-10 \cdot Q_{ss} = \frac{\partial}{\partial\eta}\left(\mathrm{Re}'\eta P H^5 \frac{\partial P}{\eta\partial\theta}\left(1 - \frac{9}{14\Lambda_0}\frac{H^2}{\eta}\frac{\partial P}{\eta\partial\theta}\right)\right)\Delta\theta\Delta\eta \tag{36}$$

If rearranging equation(36) and enforcing the expression in equation(37) back into equation(36), equation(38) can be formulated.

$$\mathrm{Re}' = \frac{\omega\rho R_i^2}{\mu_0}\left(\frac{C}{R_i}\right)^2 = \frac{\omega\rho_0 R_i^2}{\mu_0}\left(\frac{C}{R_i}\right)^2 \bar{\rho} = \mathrm{Re}'_0 P \tag{37}$$

$$-10 \cdot Q_{ss} = \mathrm{Re}'_0 \frac{\partial}{\partial\eta}\left(P^2 H^5 \frac{\partial P}{\partial\theta} - \frac{9}{14\Lambda}\frac{P^2 H^7}{\eta^2}\left(\frac{\partial P}{\partial\theta}\right)^2\right)\Delta\theta\Delta\eta \tag{38}$$

Defining a new parameter (Psi, $\Psi(\theta,\eta)$) to be equal to the mathematical expression as is shown by equation(39) to avoid the long expansion, where if done, it will be a very long term.

$$\Psi(\theta,\eta) \equiv P^2 H^5 \frac{\partial P}{\partial\theta} - \frac{9}{14\Lambda}\frac{P^2 H^7}{\eta^2}\left(\frac{\partial P}{\partial\theta}\right)^2 \tag{39}$$

Finally, the second term of the source term, equation(35) can be rewritten by equation(40). Consequently, equation(34) can be rewritten as equation(41).

$$Q_{ss} = -\frac{1}{10}\mathrm{Re}'_0 \frac{\partial\Psi(\theta,\eta)}{\partial\eta}\Delta\theta\Delta\eta \tag{40}$$

$$Q_s = 2\Lambda_0 \frac{\Delta\theta\Delta\eta}{\Delta\tau}\left(\eta PH\right) - \frac{1}{10}\mathrm{Re}'_0 \frac{\partial\Psi(\theta,\eta)}{\partial\eta}\left(\Delta\theta\right)^2\left(\Delta\eta\right)^2 \tag{41}$$

After getting both equations(39) and(41), it is possible to discretize both of them. If they are discretized following the finite element difference scheme described at the beginning of this section, they can be rewritten as equation(42) to equation(47), respectively.

$$\Psi\left(\theta,\eta\right)_{(i,j)} \equiv P^2_{(i,j)} H^5_{(i,j)} \left(\frac{P_{(i+1,j)} - P_{(i-1,j)}}{2\cdot\Delta\theta} \right) - \frac{9}{14\Lambda} \frac{P^2_{(i,j)} H^7_{(i,j)}}{\eta^2_{(i,j)}} \left(\frac{P_{(i+1,j)} - P_{(i-1,j)}}{2\cdot\Delta\theta} \right)^2 \tag{42}$$

$$\Psi\left(\theta,\eta\right)_{(i+1,j)} \equiv P^2_{(i,j)} H^5_{(i,j)} \left(\frac{-3P_{(i,j)} + 4P_{(i+1,j)} - P_{(i+2,j)}}{2\cdot\Delta\theta} \right) - \frac{9}{14\Lambda} \frac{P^2_{(i,j)} H^7_{(i,j)}}{\eta^2_{(i,j)}} \left(\frac{-3P_{(i,j)} + 4P_{(i+1,j)} - P_{(i+2,j)}}{2\cdot\Delta\theta} \right)^2 \tag{43}$$

$$\Psi\left(\theta,\eta\right)_{(i-1,j)} \equiv P^2_{(i,j)} H^5_{(i,j)} \left(\frac{+3P_{(i,j)} - 4P_{(i-1,j)} + P_{(i-2,j)}}{2\cdot\Delta\theta} \right) - \frac{9}{14\Lambda} \frac{P^2_{(i,j)} H^7_{(i,j)}}{\eta^2_{(i,j)}} \left(\frac{+3P_{(i,j)} - 4P_{(i-1,j)} + P_{(i-2,j)}}{2\cdot\Delta\theta} \right)^2 \tag{44}$$

$$Q_{s(i,j)} = 2\Lambda_0 \frac{\Delta\theta\Delta\eta}{\Delta\tau}\left(\eta P_{(i,j)} H_{(i,j)}\right) - \frac{1}{10}\cdot\mathrm{Re}'_0 \left(\frac{\Psi_{(i,j+1)} - \Psi_{(i,j-1)}}{2\cdot\Delta\eta} \right)\Delta\theta \tag{45}$$

$$Q_{s(i,j+1)} = 2\Lambda_0 \frac{\Delta\theta\Delta\eta}{\Delta\tau}\left(\eta P_{(i,j)} H_{(i,j)}\right) - \frac{1}{10}\cdot\mathrm{Re}'_0 \left(\frac{-3\Psi_{(i,j)} + 4\Psi_{(i,j+1)} - \Psi_{(i,j+2)}}{2\cdot\Delta\eta} \right)\Delta\theta\Delta\eta \tag{46}$$

$$Q_{s(i,j-1)} = 2\Lambda_0 \frac{\Delta\theta\Delta\eta}{\Delta\tau}\left(\eta P_{(i,j)} H_{(i,j)}\right) - \frac{1}{10}\cdot\mathrm{Re}'_0 \left(\frac{+3\Psi_{(i,j)} - 4\Psi_{(i,j-1)} + \Psi_{(i,j-2)}}{2\cdot\Delta\eta} \right)\Delta\theta\Delta\eta \tag{47}$$

If introducing the Peclet Number, Pe given by equation(48), (Patankar 1980), [10] on both directions (θ) and (η).

$$\frac{F^{\theta}_{i+\frac{1}{2},j}}{D^{\theta}_{i+\frac{1}{2},j}} = Pe^{\theta}_{i+1/2,j} \qquad \frac{F^{\theta}_{i-\frac{1}{2},j}}{D^{\theta}_{i-\frac{1}{2},j}} = Pe^{\theta}_{i-1/2,j} \qquad \frac{F^{\eta}_{i,j+\frac{1}{2}}}{D^{\eta}_{i,j+\frac{1}{2}}} = Pe^{\eta}_{i,j+1/2} \qquad \frac{F^{\eta}_{i,j-\frac{1}{2}}}{D^{\eta}_{i,j-\frac{1}{2}}} = Pe^{\eta}_{i,j-1/2} \quad (48)$$

Also introducing the power law scheme for numerical stability, which can be defined by equation(49).

$$A\left(\left|Pe_{i,j}\right|\right) \equiv \max\left(0, \left(1-0.1\left|Pe_{i,j}\right|\right)^{5}\right) \quad (49)$$

Now, substituting all consecutive equations from equation(30) to equation(33) and equation(41) into equation(29) With implementing Peclet Number, all expressions in equation(48), and the power law scheme, equation(49), equation(29) can be re-expressed by equation(50).

$$a_{i,j}P_{i,j} = a_{i+1,j}P_{i+1,j} + a_{i-1,j}P_{i-1,j} + a_{i,j+1}P_{i,j+1} + a_{i,j-1}P_{i,j-1} + b_{i,j} \quad (50)$$

, where

$$a_{i+1,j} = D^{\theta}_{i+1/2,j}A\left(\left|Pe^{\theta}_{i+1/s,j}\right|\right)$$

$$a_{i-1,j} = D^{\theta}_{i-1/2,j}\left[A\left(\left|Pe^{\theta}_{i-1/s,j}\right|\right) + Pe^{\theta}_{i-1/s,j}\right]$$

$$a_{i,j+1} = D^{\eta}_{i,j+1/2}A\left(\left|Pe^{\eta}_{i,j+1/s}\right|\right)$$

$$a_{i,j-1} = D^{\eta}_{i,j-1/2}\left[A\left(\left|Pe^{\eta}_{i,j-1/s}\right|\right) + Pe^{\eta}_{i,j-1/s}\right]$$

$$a_{i,j} = a_{i+1,j} + a_{i-1,j} + a_{i,j+1} + a_{i,j-1} + \max\left(0, \left(F_{i+1/2,j} - F_{i-1/2,j} + F_{i,j+1/2} - F_{i,j-1/2}\right)\right) + \eta_{i,j}\frac{2\Lambda\Delta\theta\Delta\eta}{\Delta\tau}\left(H_{i,j}\right)_{AV}$$

$$b_{i,j} = \max\left(0, \left(-F_{i+1/2,j} + F_{i-1/2,j} - F_{i,j+1/2} + F_{i,j-1/2}\right)\right)\overline{P}_{i,j} + Q_{s(i,j)}$$

Thus, equation(50) is the discretized form of the Non-Dimensional Modified Reynolds Equation, noting that while incorporating these equations in the code, if statements should be made where both the terms of $Q_s(i,j)$ and $\Psi(\theta,\eta)_{(i,j)}$ embedded inside it should be reflected and considered in the term $b_{i,j}$ based on the location of the grid points.

Mesh Refinement

Both Table 3 and Table 4 show the cases of mesh refinement for the case of rigid Hydrodynamic bearing of 3-bar and 9-bar ambient pressures, respectively. These two cases have been chosen to do a refinement study to choose an optimal grid point for doing the numerical computation. The rigid hydrodynamic case has been chosen to do the refinement analysis because it is the fastest case where the results could be simulated with just a button click. The chosen grid points, highlighted in gray, are the 120 and 60 grid points along the circumferential and radial directions, respectively. This meshing option has been chosen to be an optimal option for this analysis because it maintains a good accuracy of the results as it is possible to see the comparison within the upcoming paragraphs, and it does not take a very long time for the numerical solution to be computed, especially for foil bearing cases.

The main objective of the numerical analysis in this thesis is to make a comparison between both solutions of the classical Reynolds equation – the inertia effect not considered – versus the modified Reynolds equation, where the inertia effect is considered. Therefore, it really matters how to choose the grid points while doing the simulation because it highly affects the solution accuracy. Since the key parameter that should be solved first from these equations is the pressure, and the load capacity is mainly the required parameter to be compared from both solutions, both are assigned to be compared while doing the refinement study of the grid points.

If looking through the tables below, one can see that the difference between both values of the pressure when including and not including the inertia terms (Pressure Difference, in the tables) are decreasing as the grid points are increased. This means that the accuracy of the results is getting better. Further, if we look at Table 3, the schemes of grid points, one can see that the difference between both values of the pressure difference of the current chosen grid point and the

next choice of a grid point is approximately between $0.0055 \sim 0.01$ bar. Similarly, if one look at the difference between the difference of the load capacity of the current grid point and the next grid point choice, it is possible to see that the difference is ranging between $0.7 \sim 2.50$ N. If considering the refinement study based on the ambient pressure equals to 3 bar, the study will not be accurate and not accurate to do the comparison because in the case of rigid hydrodynamic case, it was barely to see a difference between both solutions of including and not including the inertial terms when the ambient pressure is less or equal to 3 bar. Therefore, a higher ambient pressure condition, 9 bar, has been chosen to further investigate and complete this refinement study. If looking at Table 4, it is possible to see that the difference between both values of the pressure difference of the current chosen grid point and the next choice of a grid point is approximately between $0.0082 \sim 0.06$ bar. Similarly, if one look at the difference between the difference of the load capacity of the current grid point and the next grid point choice, it is possible to see that the difference is ranging between $4.50 \sim 15$ N. Accordingly, it is possible to infer that the higher the grid points, the higher the accuracy of the output results. However, the choice of the grid point should be picked wisely because a great deal of time is required when solving for both cases of foil bearing, where the transient method should be used due to the deflection of the bearing's foil. Consequently, the current chosen number of grid points highlighted in gray in both tables is an optimal choice, and there is no need to increase the number of grid points further because it has been noted several times when the grid points are increased to a level more than the current choice of grid points, highlighted in gray, the required time for the computation is dramatically increased. Therefore, no need to go to higher grid points, especially that the difference of the pressure difference and the load capacity difference of each grid point choice and its next grid point choice is almost nothing. Furthermore, these differences between solutions are not worthy to increase the

computational time, especially if the simulation will be run several times to solve for all ambient pressures ranging from 1 to 10 bar.

Table 3: Grid points refinement for rigid hydrodynamic 3 bar ambient pressure

Grid Points(n)	Grid Points(m)	Maximum Pressure (bar)		Pressure Difference	Load Capacity (N)		Load Capacity Difference
		No Inertia	Inertia		No Inertia	Inertia	
30	15	10.2487	10.1619	0.0868	1218.83	1199.52	19.31
60	30	10.1653	10.0853	0.0800	1143.27	1125.96	17.31
90	45	10.1266	10.0525	0.0741	1115.91	1099.34	16.57
120	60	10.0356	9.96697	0.0686	1087.43	1072.10	15.33
150	75	9.82918	9.76782	0.0614	1039.10	1025.83	13.27
180	90	9.53879	9.48683	0.0520	975.836	964.786	11.05
210	105	9.21838	9.17514	0.0432	907.170	898.051	9.119

Table 4: Grid points refinement for rigid hydrodynamic 9 bar ambient pressure

Grid Points(n)	Grid Points(m)	Maximum Pressure (bar)		Pressure Difference	Load Capacity (N)		Load Capacity Difference
		No Inertia	Inertia		No Inertia	Inertia	
30	15	18.4296	17.8990	0.5306	1431.53	1296.41	135.12
60	30	18.2356	17.7306	0.5050	1319.99	1199.08	120.91
90	45	18.1668	17.6700	0.4968	1282.67	1166.26	116.41
120	60	18.0647	17.5949	0.4698	1247.74	1138.84	108.9
150	75	17.8621	17.4363	0.4258	1190.22	1093.68	96.54
180	90	17.5810	17.2076	0.3734	1110.90	1028.03	82.87
210	105	17.2671	16.9432	0.3239	1017.75	946.595	71.155

Chapter 4: RESULTS AND DISCUSSION

After discretizing the Modified Reynolds Equation as fully explained in detail in the previous chapter, the next step is to implement all equations from the prior chapter to the C++ code. After implementing, debugging, and making sure that the results were converging, and the results were satisfactory, they agreed to the former literature in chapter 2, the code was run again several times to simulate the case of both rigid and foil thrust bearings. This simulation has been done with the consideration of the incompressible lubricant, isothermal medium, and constant viscosity because the main aim is to purely investigate the effects of the inertia effects (Centrifugal Force) when added to the classical lubrication equation (Reynolds Equation).

Results from Simulation

Several cases were run to simulate the thrust bearing that has the parameters given in chapter 1, Table 1 as rigid and foil bearing. Both lubrication modes of hydrodynamic as well as hybrid are simulated for both types of bearing. When simulating for the rigid mode, the minimum film thickness is set to be constant at 5 microns and used to be the input in the Reynolds equation solver. Therefore, after the pressure has been calculated, it will be integrated over the pad's area to get the load capacity of the bearing. With that being done, after simulating both cases with including and without including the inertia effect, it is possible to see the difference and do the comparison through the maximum local Reynolds number, pressure profiles, streamlines, deflections, and load capacity. However, different step input external load is applied until achieving approximately the 5 microns minimum film thickness when simulating for the foil bearing case.

Local Reynolds Number

The bearing has been simulated up to 10 bar (1000 kPa) ambient pressure to mainly measure the bearing's load capacity. The simulation cases were limited to 10 bar ambient pressure because this limitation was based on the calculation of the local Reynolds number. The calculation of the local Reynolds number is given by equation(51). Table 5 shows the maximum local Reynolds numbers at the grid points for all simulated cases. This calculation has been done to verify that the maximum local Reynolds number at the grid points is around 2300 as an indicated measure for this solution to be valid since the main assumption was based on Laminar flow. Cengel, Y. and Cimbala, J. have stated that for a flow to be a laminar flow, Reynolds number should be smaller or equal to 2300. It is a transitional flow if the Reynolds number is greater or equal to 2300 and smaller or equal to 4000; however, the flow is turbulent if the Reynolds number is greater than 4000, [12].

$$\mathrm{Re} = \frac{p(r,\theta)h(r,\theta)\bar{u}_{\theta}(r,\theta)}{R_{gas}T\mu} \tag{51}$$

, where $\bar{u}_{\theta}(r,\theta)$: is the average circumferential velocity given by equation(52)

$P(r,\theta)$: is the pressure over the pad area.

$h(r,\theta)$: is the film thickness, and here it considered to be the hydraulic diameter.

R_g : is the gas constant T: is the temperature μ : is the dynamic viscosity

Generally, Table 5 shows that the local Reynolds number is getting higher as the pressure increases and tends to be almost similar for both cases of Rigid hydrodynamic bearing whether including or not including the inertia effect. Nevertheless, in the case of the Rigid hybrid bearing, the local Reynolds number tends to get a bit smaller when including the inertia effect.

Unlikely, for both cases of the lubrication mode of the foil bearing, the local Reynolds number tends to increase with including the inertia terms and even get higher than 3000 when the pressure is 8, 9, and 10 bar in the case of foil hybrid. Even though the pressure drops as explained in detail in the following section when including the inertia terms, the increase of the average velocity along the circumferential direction causes the local Reynolds number to get higher due to the proportionality with the average velocity in equation(51). However, in the hydrodynamic case is not obvious as in hybrid mode because the pressure gradient is smaller if both cases are compared. Looking at equation(52) and equation(53), it is possible to see that their terms are dependent on the pressure gradient. Therefore, both velocities are getting larger while operating the hybrid mode. Therefore, this is obvious if the bearing's foils deflect, that will cause a higher clearance (gap), which, in turn, causes a higher volumetric flow rate and velocity based on the following mathematical relation, $Q = Av$. The pressure keeps building up gradually to a very high level at the location around the orifices, or perhaps at the tapered region, and that, in turn, will cause the sagging effect of the foils in case of the foil bearing and a high leakage flow along the tapered region. Consequently, the local Reynolds number difference is larger between both cases of the foil bearing. All these details will be discussed further in the following two sections.

The flow of these foil-bearing cases at high pressures might still be laminar because the tabulated local Reynolds numbers have been identified to be the maximum at the injection orifices for the hybrid cases, at which the flow is very high. Besides, these local Reynolds numbers are in the range of the transitional flow, and there is a 50% chance that the flow is still laminar since the streamlines are smooth and regular, and they do not break up. According to Johns (2017)," laminar flow, in which the streamlines are smooth and regular. Unlikely, turbulent flow, in which the

streamlines break up (p. 73)," [11]. Therefore, if the plots of the streamlines are examined in the section on the velocities and streamlines, one can see that those streamlines are smooth and regular.

Table 5: Maximum local Reynolds numbers at the grid points for all simulation cases

Pressure (bar)	Maximum Value of Local Reynolds Number							
-	Rigid Hydrodynamic		Rigid Hybrid		Foil Hydrodynamic		Foil Hybrid	
-	Without Inertia	With Inertia	Without Inertia	With Inertia	Without Inertia	With Inertia	Without Inertia	With Inertia
1	142.3	142.3	365.89	365.855	137.77	137.788	405.21	409.226
2	284.599	284.599	680.687	680.459	273.003	273.219	810.047	812.898
3	426.899	426.899	950.53	949.863	407.882	408.729	1164.12	1170.96
4	569.199	569.199	1205.59	1204.34	542.448	545.423	1520.52	1533.54
5	711.498	711.498	1455.77	1453.78	678.109	682.555	1878.45	1900.29
6	853.798	853.798	1702.83	1699.96	814.393	821.262	2238.72	2272.3
7	996.098	996.098	1947.73	1943.85	950.724	981.497	2601.3	2650.76
8	1138.4	1138.4	2191.09	2186.1	1087.2	1123.34	2965.76	3024.5
9	1280.7	1280.7	2433.29	2427.14	1224.33	1241.52	3331.54	3400.85
10	1423	1424.38	2674.62	2667.26	1361.19	1369.01	3719.26	3796.24

Pressure

The pressure is the key parameter for bearing simulation as stated by Michel Khonsari in his book, [9]. The pressure has been plotted for all four cases of the thrust bearing at different ambient pressures. The cases of 3, 6, and 9 bar will be discussed further throughout this section. Figure 8, Figure 9, and Figure 10 illustrate the pressure distribution of the rigid bearing cases for 3, 6, and 9 bar, respectively. Whereas Figure 11, Figure 12, and Figure 13 show the pressure distribution of the Foil bearing cases for 3, 6, and 9 bar, respectively. If one looks closely at these plots, it is always true that the hybrid mode has higher pressure distribution along the bearing's pads' area than those of the hydrodynamic mode because of the externally supplied lubricant to

the system. The rigid bearing always surpasses the foil bearing in having the higher-pressure distribution due to the high rigidity (zero deflection assumption). However, the foil bearing has its foils to be deflected, and that is obvious through the corrugations on the surfaces of the pressure profiles as illustrated in the foil bearing figures. Moreover, it is noticeable there is a pressure drop when including the inertia terms. The maximum values of the pressures between every two cases when not including and including the inertial terms are tabulated in Table 6 and Table 7, respectively. From both Table 6 and Table 7, it is possible to see that the maximum pressure gets higher as the ambient pressure increases. The difference between the two maximum values from both tables for each pressure case is getting higher as the ambient pressure increases for the rigid as well as the foil bearing. There is a noticeable difference in the case of the rigid bearing and the difference tends to be insignificant if comparing both lubrication modes of the rigid bearing due to no deflection. Therefore, there is no big difference whether to supply more lubricant to the system or not. However, in the case of the foil bearing, the difference between the maximum pressures from both tables for each pressure case is getting more noticeable, and this difference gets even higher in case of the hybrid mode due to the higher deflection of the bearing's foils. The amount of deflections is getting higher in the case of hybrid mode due to the externally supplied lubricant to the system, and the deflection increases with the increase of the pressure. This can be seen from Figure 30, Figure 31, and Figure 32. If one compares the difference between the maximum pressures for each case of both lubrication modes of the foil bearing, one can see that this difference gets more distinguishable for the case of foil bearing than it was in the rigid bearing case due to the increase of the pressure and the deflection simultaneously as more lubricant is supplied to the system.

Pressure Profiles of Rigid Bearing Case

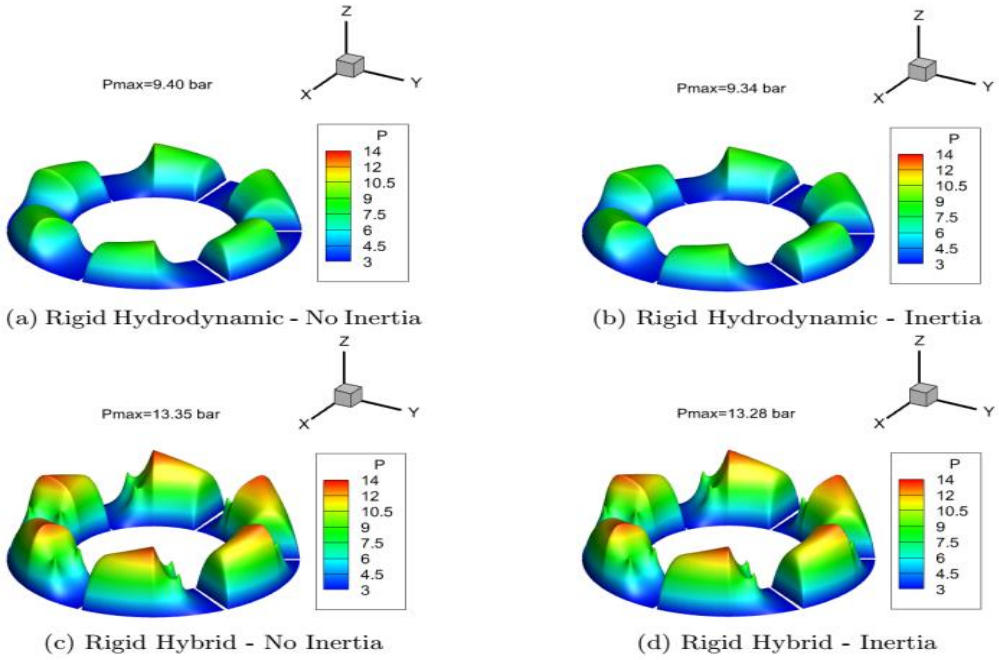

(a) Rigid Hydrodynamic - No Inertia (b) Rigid Hydrodynamic - Inertia

(c) Rigid Hybrid - No Inertia (d) Rigid Hybrid - Inertia

Figure 8: Pressure distribution profiles of the rigid bearing six pads, P=3bar

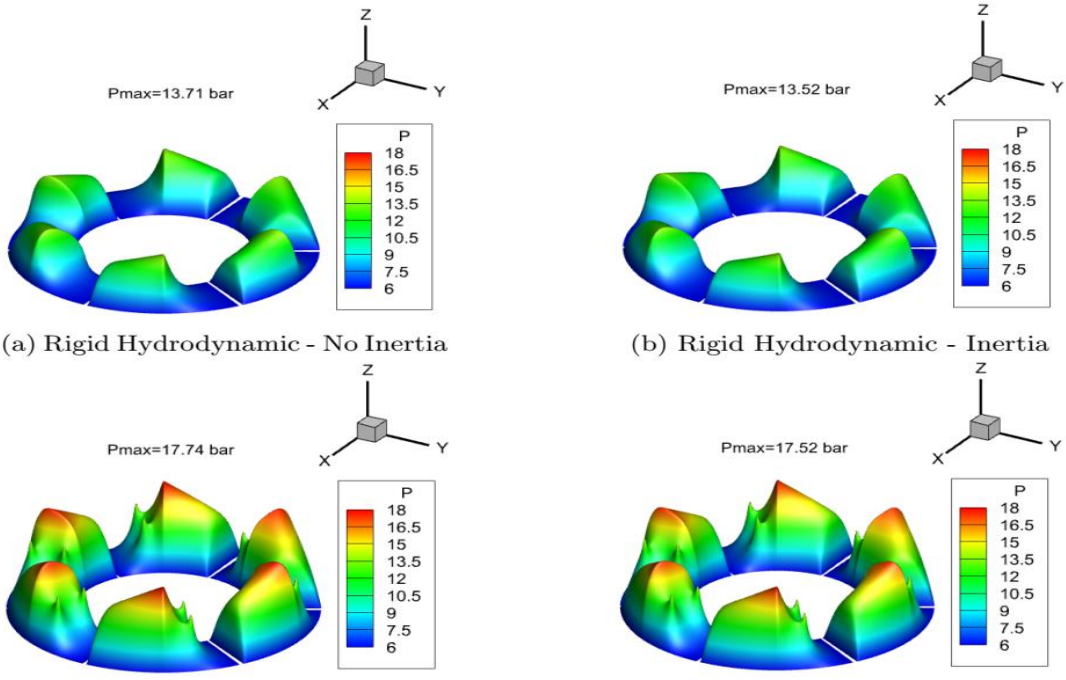

(a) Rigid Hydrodynamic - No Inertia (b) Rigid Hydrodynamic - Inertia

(c) Rigid Hybrid - No Inertia (d) Rigid Hybrid - Inertia

Figure 9: Pressure distribution profiles of the rigid bearing six pads, P=6bar

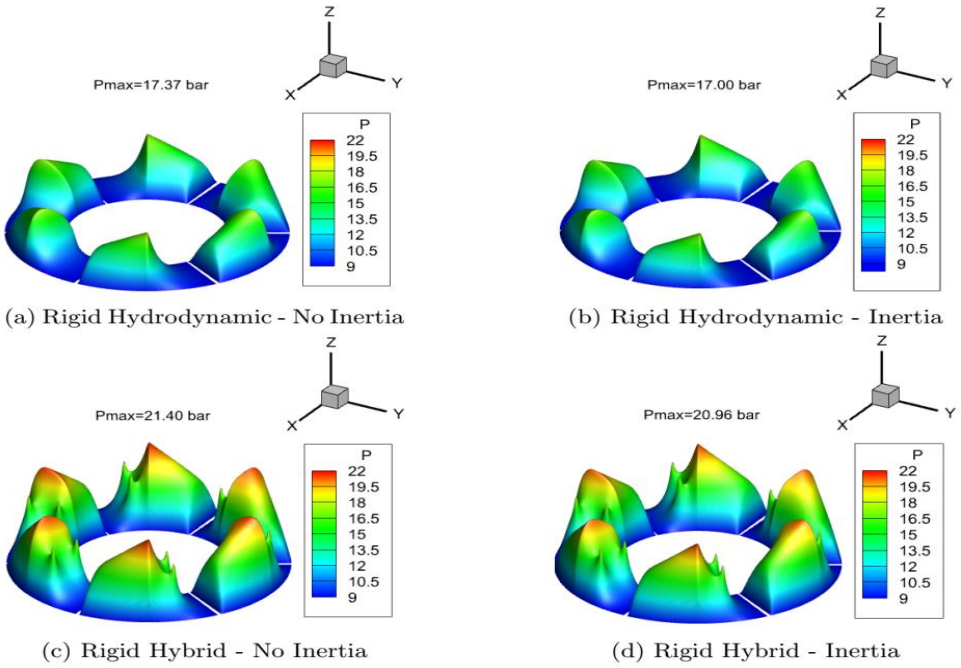

(a) Rigid Hydrodynamic - No Inertia (b) Rigid Hydrodynamic - Inertia

(c) Rigid Hybrid - No Inertia (d) Rigid Hybrid - Inertia

Figure 10: Pressure distribution profiles of the rigid bearing six pads, P=9bar

Pressure Profiles of Foil Bearing Case

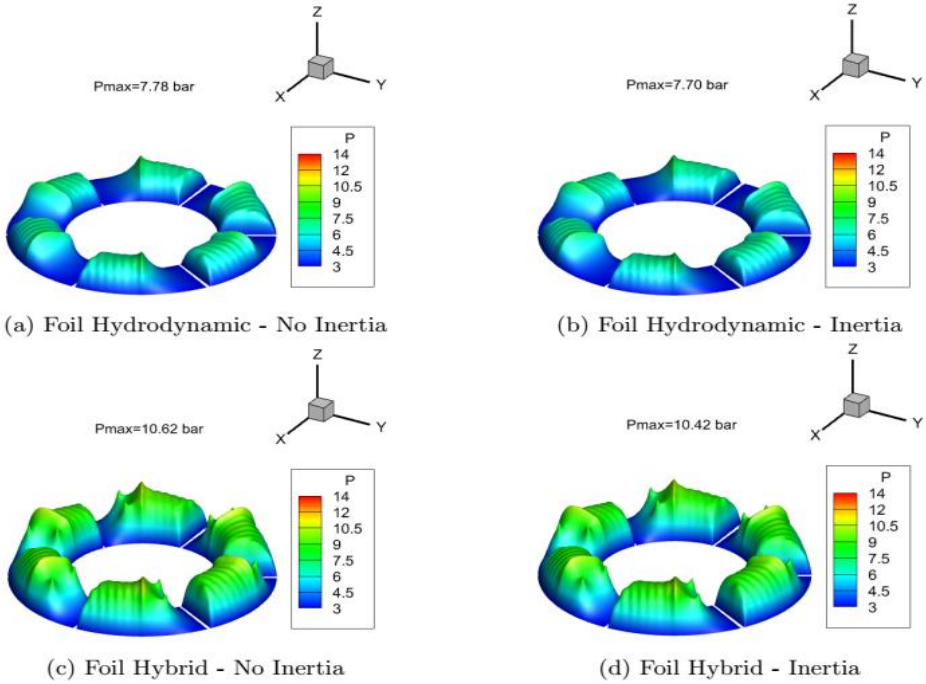

(a) Foil Hydrodynamic - No Inertia (b) Foil Hydrodynamic - Inertia

(c) Foil Hybrid - No Inertia (d) Foil Hybrid - Inertia

Figure 11: Pressure distribution profiles of the foil bearing's six pads, P=3bar

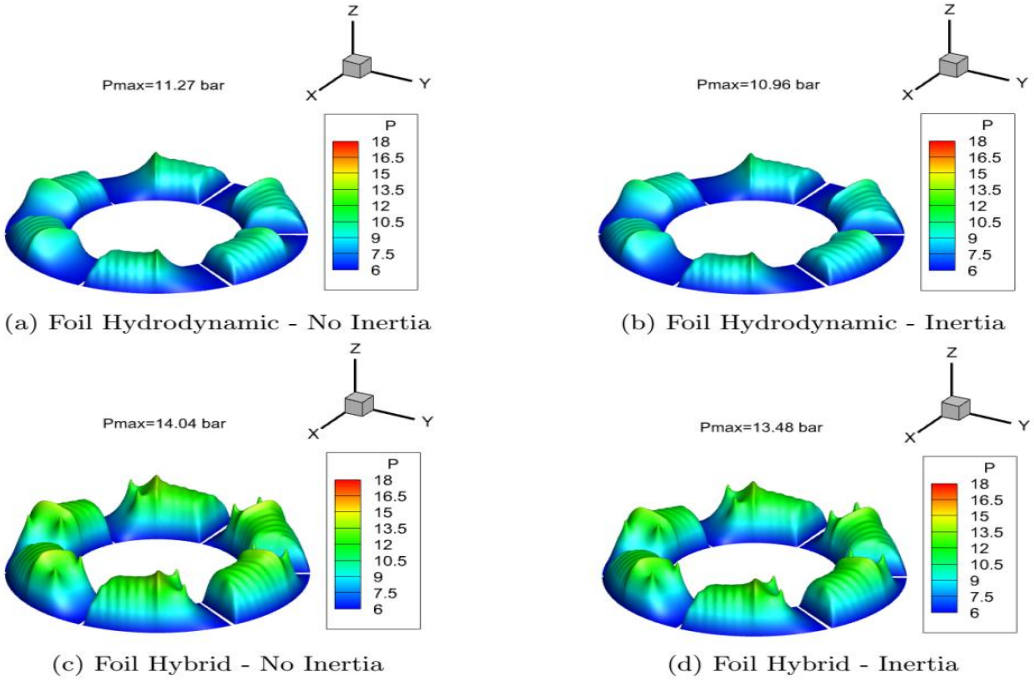

(a) Foil Hydrodynamic - No Inertia (b) Foil Hydrodynamic - Inertia

(c) Foil Hybrid - No Inertia (d) Foil Hybrid - Inertia

Figure 12: Pressure distribution profiles of the foil bearing six pads, P=6bar

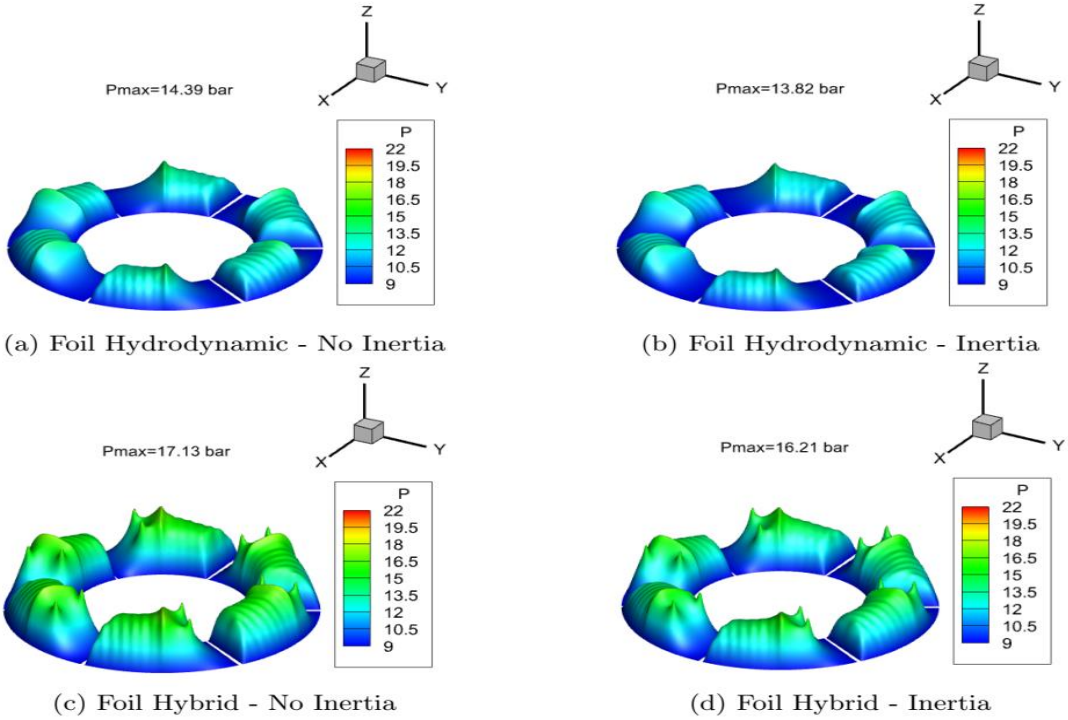

(a) Foil Hydrodynamic - No Inertia (b) Foil Hydrodynamic - Inertia

(c) Foil Hybrid - No Inertia (d) Foil Hybrid - Inertia

Figure 13: Pressure distribution profiles of the foil bearing six pads, P=9bar

Table 6: Maximum pressure of cases without including inertia terms

-	Rigid Hydrodynamic	Rigid Hybrid	Foil Hydrodynamic	Foil Hybrid
Pressure (bar)	Maximum Pressure			
3	9.40	13.35	7.78	10.62
6	13.71	17.74	11.27	14.04
9	17.37	21.40	14.39	17.13

Table 7: Maximum pressure of cases with including inertia terms

-	Rigid Hydrodynamic	Rigid Hybrid	Foil Hydrodynamic	Foil Hybrid
Pressure (bar)	Maximum Pressure			
3	9.34	13.28	7.70	10.42
6	13.52	17.52	10.96	13.48
9	17.00	20.96	13.82	16.21

Velocities and Streamlines

One of the extremely important matters that should be investigated when studying the lubrication of the thrust bearing is to look at how the lubricant particles are moving through the bearing's medium. The family of Streamlines is a very good option to trace the movement of the fluid particles since the velocity vectors will almost always be tangent to these lines. If one integrates both equations(13) and(14) over the film thickness h, it is possible to obtain both equations(52) and(53), which are the average velocities of *u* and *v*, respectively.

$$\bar{u}_\theta(r,\theta) = \frac{r\omega}{2} - \frac{1}{12}\frac{h^2}{r\mu}\frac{\partial p}{\partial \theta} \tag{52}$$

$$\bar{v}_r(r,\theta) = -\frac{1}{12}\frac{h^2}{\mu}\frac{\partial p}{\partial r} + \frac{1}{12}\frac{\rho r\omega^2 h^2}{\mu} + \frac{1}{4}\frac{\rho K_1 h^3}{\mu r} + \frac{3}{10}\frac{\rho K_2 h^4}{\mu r} + \frac{1}{3}\frac{\rho K_3 h^5}{\mu r} + \frac{5}{14}\frac{\rho K_4 h^6}{\mu r} \tag{53}$$

Using both above equations, it is possible to generate the following streamlined plots. If one looks closely at the next figures representing the streamlines, one can see that the velocity vector along the circumferential direction is always dominant, especially at the flat region which is located on the right-hand side from the center of the figures, specifically at the right of the notation of $\theta_{taper} = 29$, along the horizontal axis. This velocity vector is generated due to the moving surface relative to the stationary surface, which is known as the *Couette flow*. Figure 14, Figure 15, and Figure 16 show the streamlines of the rigid hydrodynamic bearing for the pressure equal to 3bar, 6bar, and 9bar, respectively. Moreover, Figure 18, Figure 19, and Figure 20 illustrate the streamlines of the foil hydrodynamics bearing for the pressure equal to 3bar, 6bar, and 9bar, respectively. All these figures show that the velocity vectors (v_r) along the radial direction are getting higher at the top and bottom left corners. Therefore, the streamlines get curved toward the north direction at the top corners and toward the south direction at the bottom corners. This happens because of the flow associated with the pressure gradient along the radial direction, which is the first term of equation(53). Therefore, it is possible to see that those curved streamlines are getting a bit wider toward the center of the bearing's pads along the circumferential direction as the pressure increases. It is possible to see this behavior through Figure 17, and Figure 21, where all three pressure cases are illustrated when the inertia effect is not included, especially comparing the Pb=3 bar to the Pb=6 bar or Pb=9 bar. Likely, this is also happening for the case when including the inertia terms. In addition, there is also an extra effect of the other terms of equation(53) when including the inertia effect that may responsible to change the intensity of the average velocity along the radial direction ,and that is based on the value of the pressure gradient along the circumferential direction. However, Figure 22, Figure 23, and Figure 24 illustrate the streamlines of the rigid hybrid bearing for the pressures of 3 bar, 6 bar, and 9 bar, respectively. Further, Figure

26, Figure 27, and Figure 28 show the streamlines of the foil hybrid bearing for the pressures of 3 bar, 6 bar, and 9 bar, as well. All these figures show that the externally injected air is involved in the case of the hybrid mode through the two orifices at the tapered region through which the air is gushing out. Noteworthy, the flow along the circumferential direction dominates the flow throughout the medium, except at the region of the orifices. Mainly, the flow should be a summation of both the *Couette flow* as well as the pressure gradient flow along the circumferential direction. Nevertheless, in the tapered region, it is possible to realize that the pressure gradient along both directions gets to a high level due to the externally injected lubricant. As previously stated above for the case of the hydrodynamic bearing, when the inertia terms are included, there will be an additional effect on the radial velocity component, where the intensity of the flow may change. Through the tapered region exactly just after the leading edge, it is possible to notice that the streamlines get a bit more squeezed or crumpled when not including the inertia terms, and this gets more noticeable for the 6, and 9 bar cases as that can be clearly shown through Figure 25. Moreover, the streamlines even go in the reverse direction due to the dominance of pressure gradient along the circumferential direction at the leading edge as clearly shown in Figure 29, where all three different pressures can be compared for the foil bearing case when the inertia effect is not included. This is happening because the bump foil is sagging and deflecting a bit more when inertia terms are not included due to the higher pressure. Noticing that, at the tapered region, the highest deflection occurs as shown in Figure 30, Figure 31, and Figure 32. However, when adding the inertia terms, the deflection of the bump foil is a bit less because the pressure is lower, where the leakage flow is higher. From another perspective, this is reasonable because the velocities get higher when including the inertia terms, and it is possible to see that from the calculated local Reynolds numbers in Table 5.

Streamlines of Rigid & Foil Hydrodynamic Bearing Cases

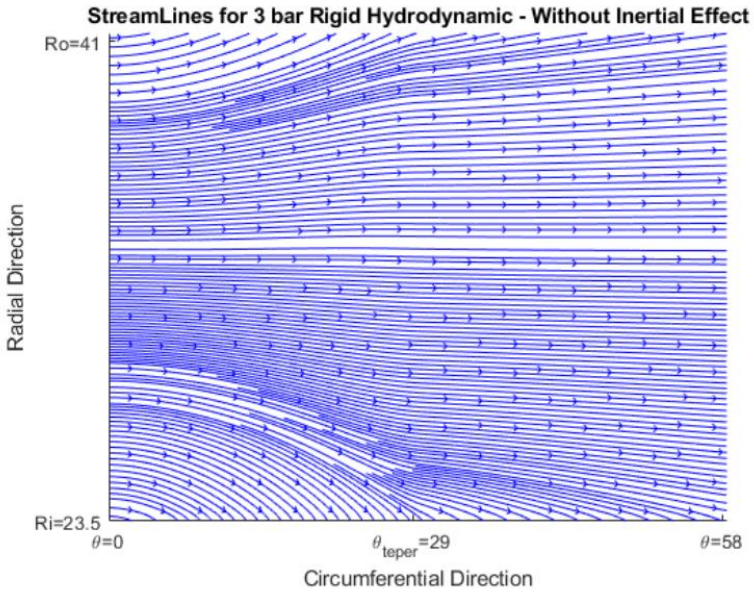

(a) Rigid Hydrodynamic - No Inertia

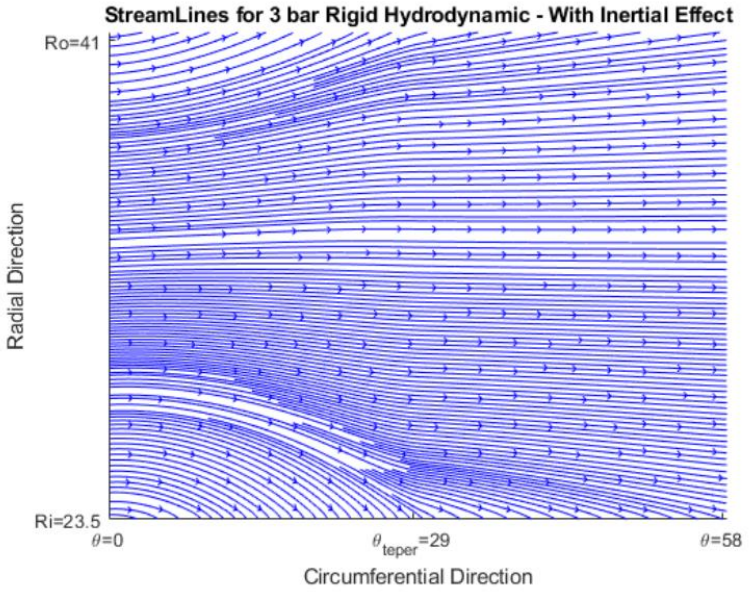

(b) Rigid Hydrodynamic - Inertia

Figure 14: Rigid hydrodynamic streamlines, P=3bar

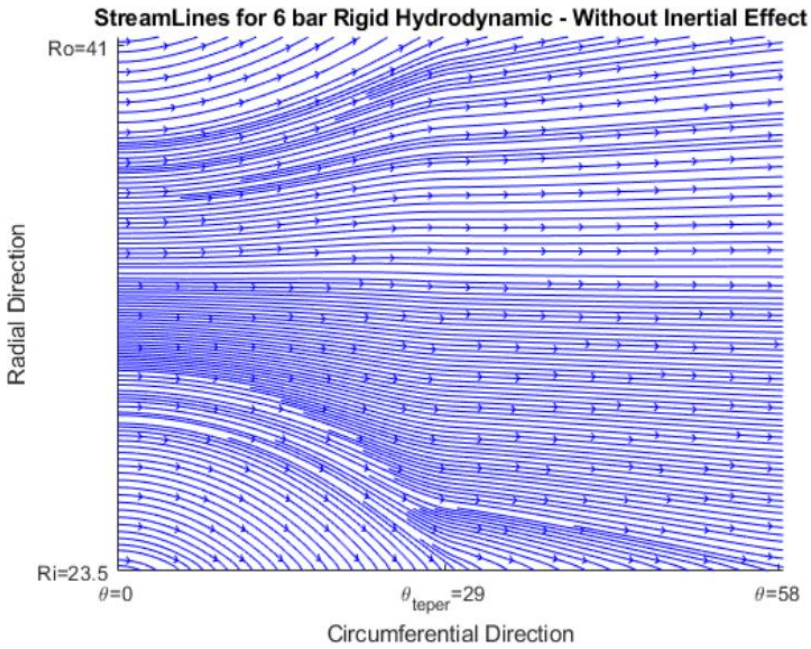

(a) Rigid Hydrodynamic - No Inertia

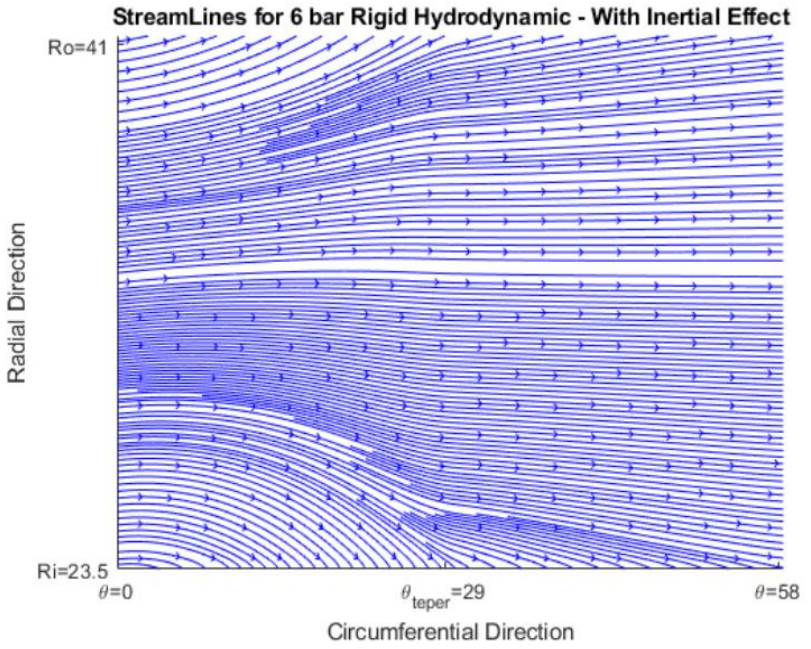

(b) Rigid Hydrodynamic - Inertia

Figure 15: Rigid hydrodynamic streamlines, P=6bar

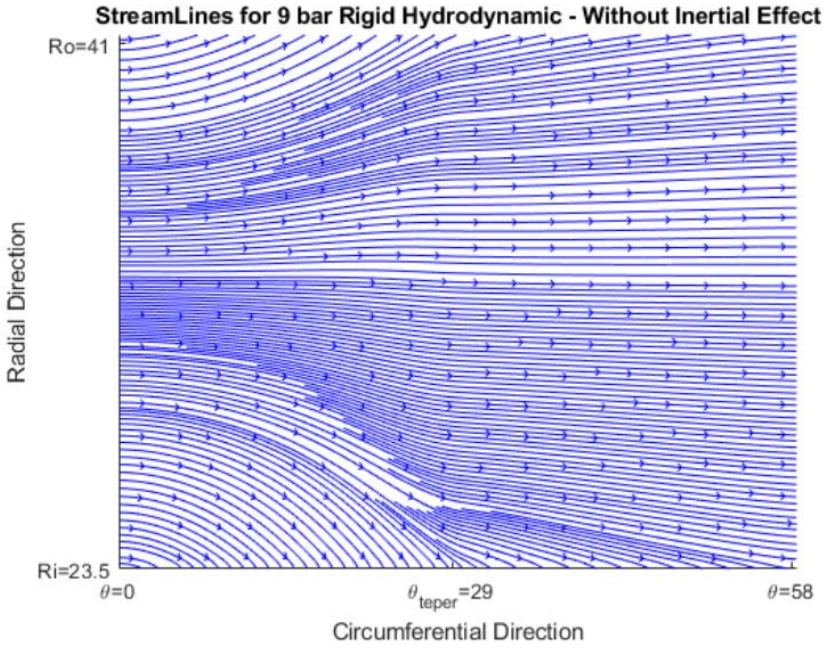

(a) Rigid Hydrodynamic - No Inertia

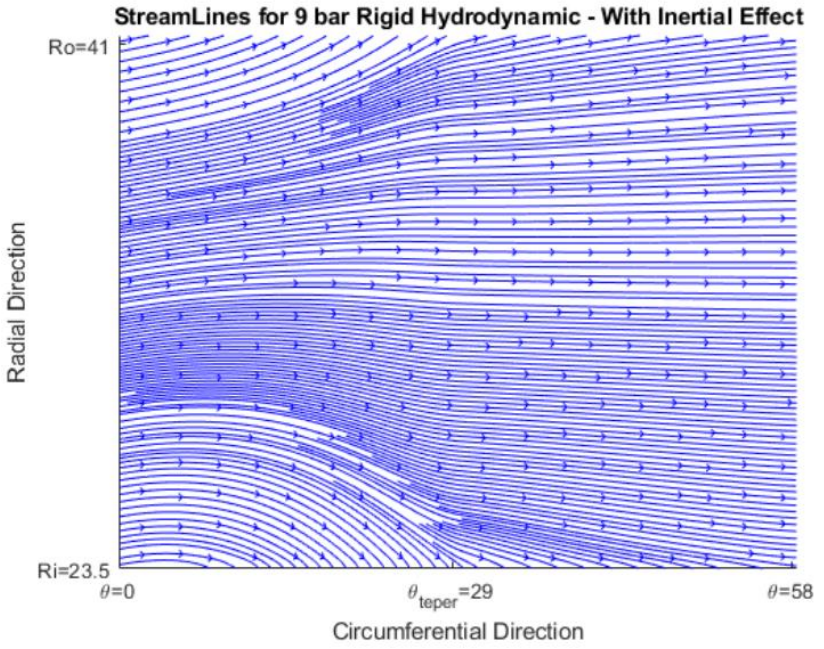

(b) Rigid Hydrodynamic - Inertia

Figure 16: rigid hydrodynamic streamlines, P=9bar

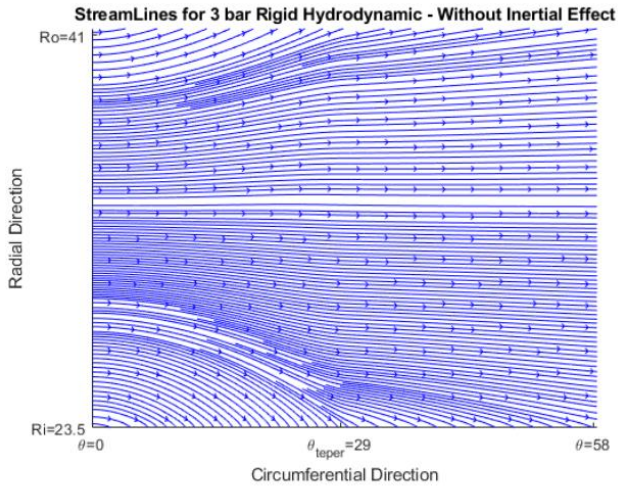

(a) Pb=3 bar

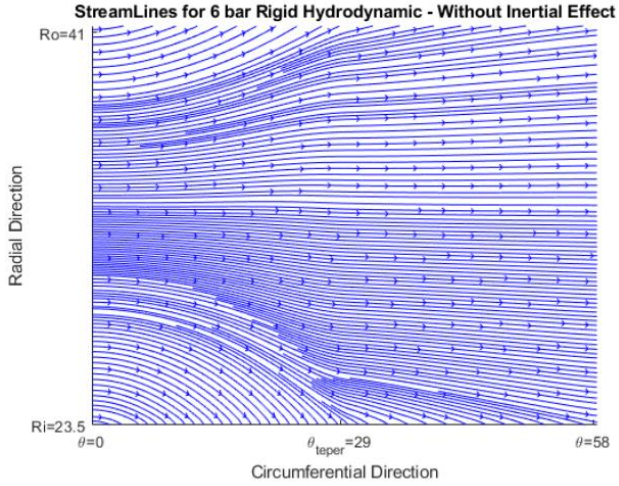

(b) Pb=6 bar

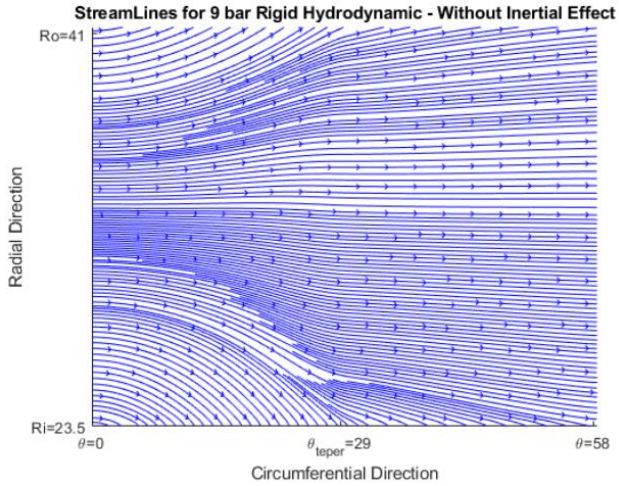

(c) Pb=9 bar

Figure 17: Rigid hydrodynamic streamlines for all three cases -no Inertia

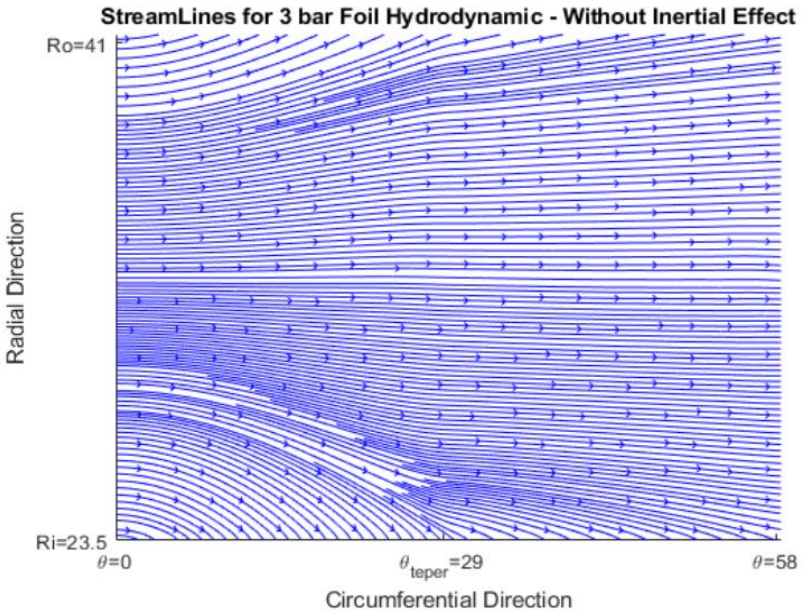

(a) Foil Hydrodynamic - No Inertia

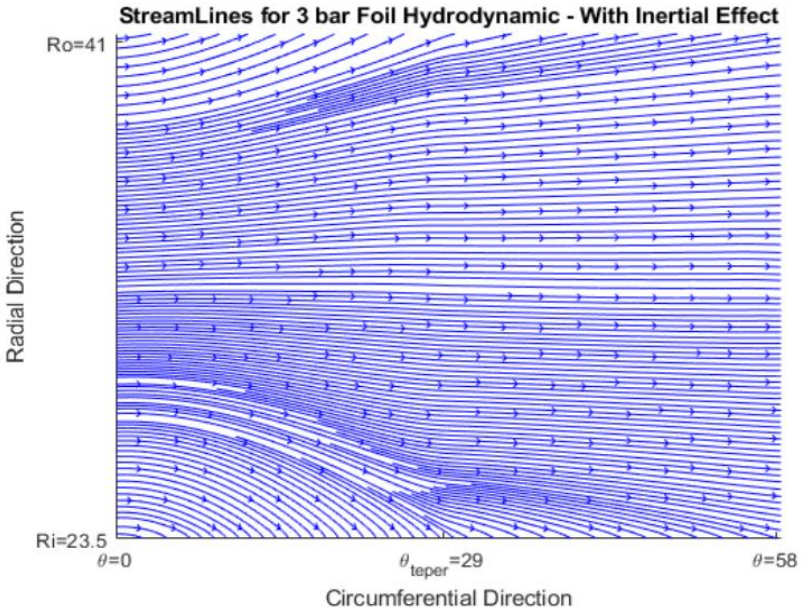

(b) Foil Hydrodynamic - Inertia

Figure 18: Foil hydrodynamic streamlines, P=3bar

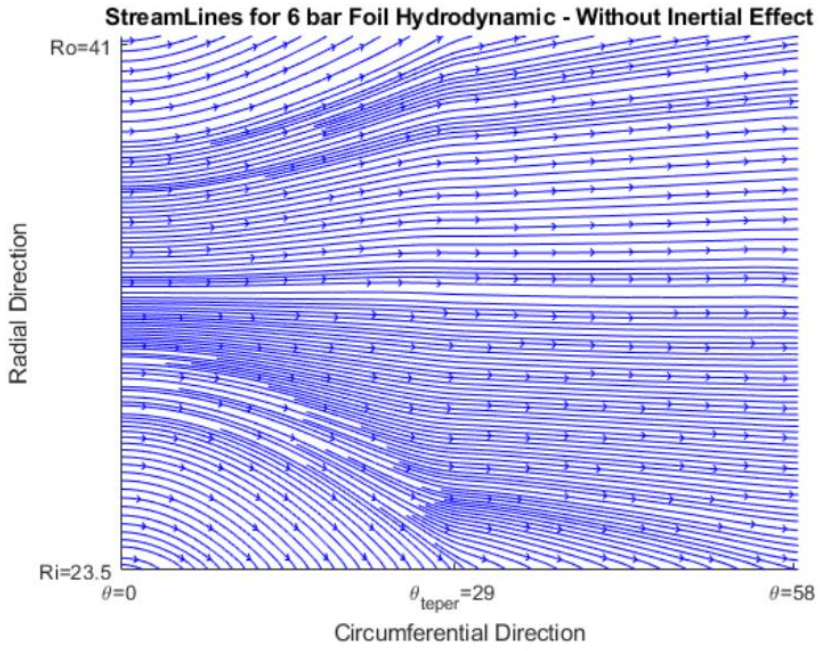

(a) Foil Hydrodynamic - No Inertia

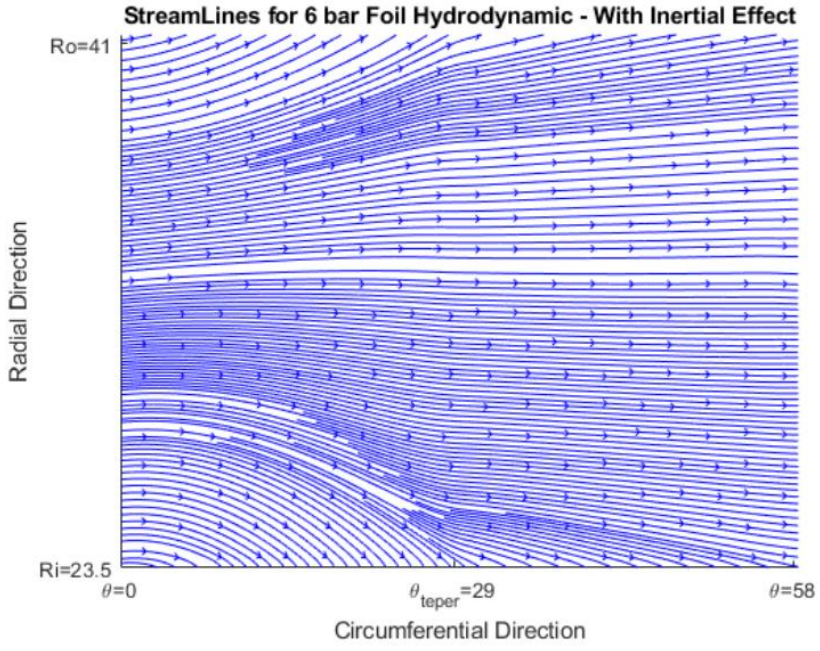

(b) Foil Hydrodynamic - Inertia

Figure 19: Foil hydrodynamic streamlines, P=6bar

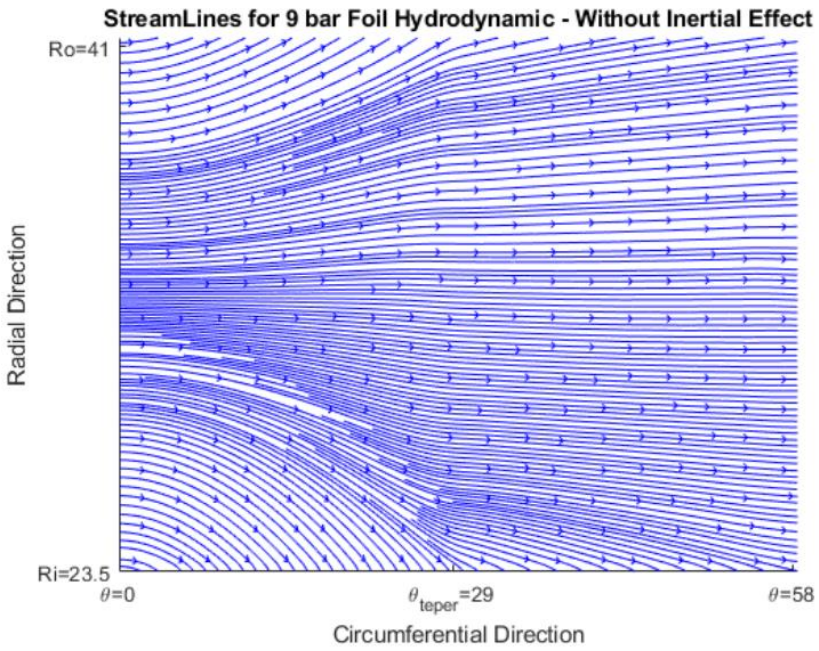

(a) Foil Hydrodynamic - No Inertia

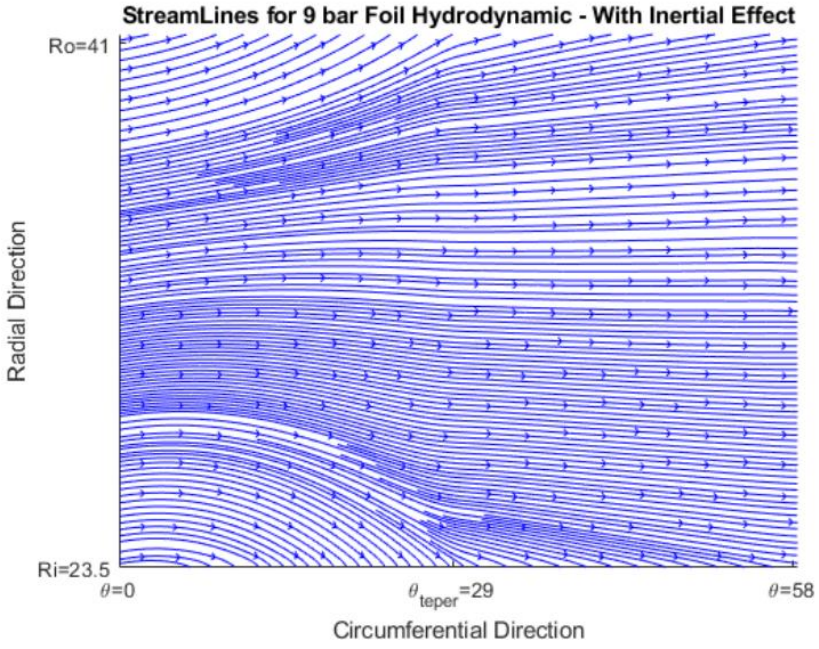

(b) Foil Hydrodynamic - Inertia

Figure 20: Foil hydrodynamic streamlines, P=9bar

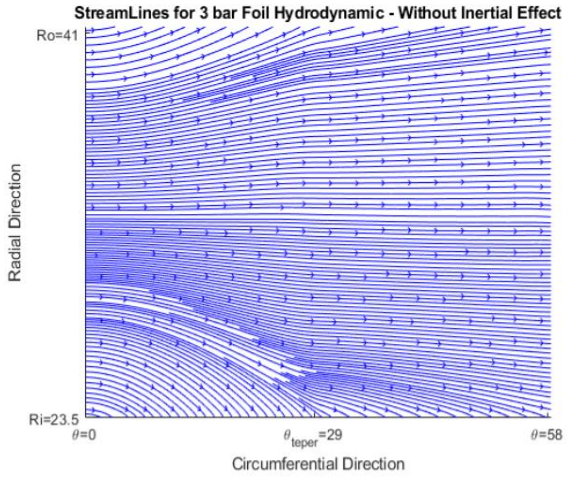

(a) Pb=3 bar

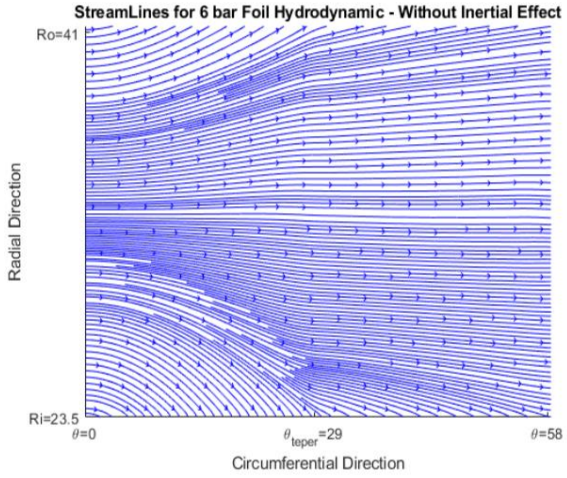

(b) Pb=6 bar

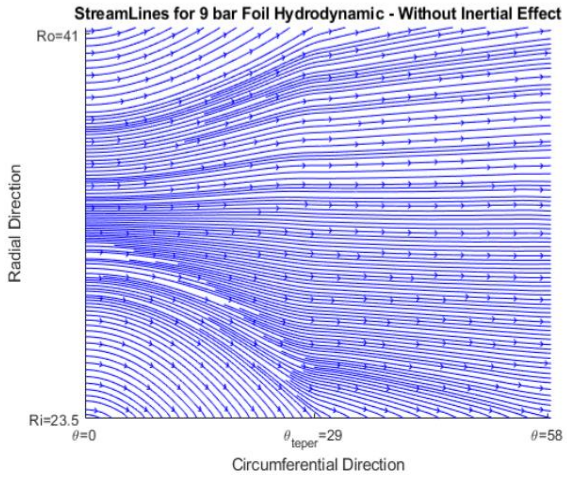

(c) Pb=9 bar

Figure 21: Foil hydrodynamic streamlines for all three cases – no Inertia

The Streamlines' Figures of Rigid & Foil Hybrid Bearing Cases

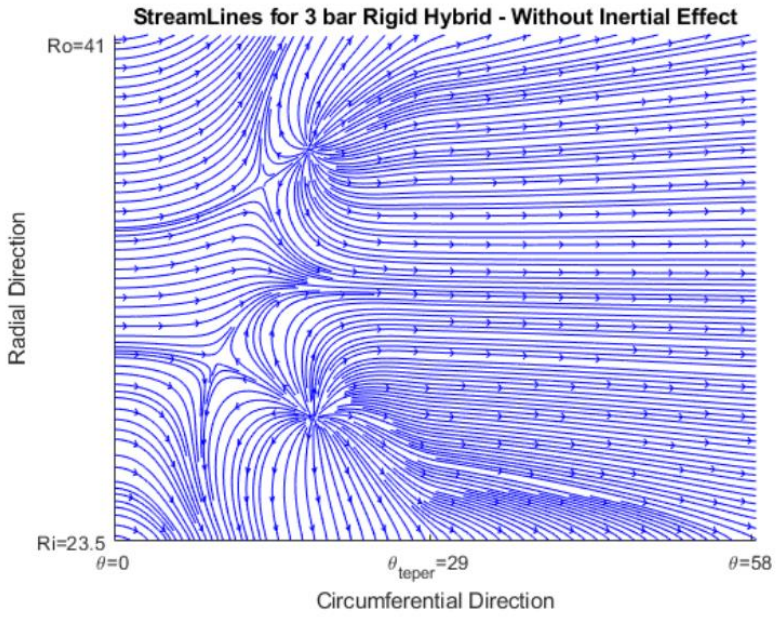

(a) Rigid Hybrid - No Inertia

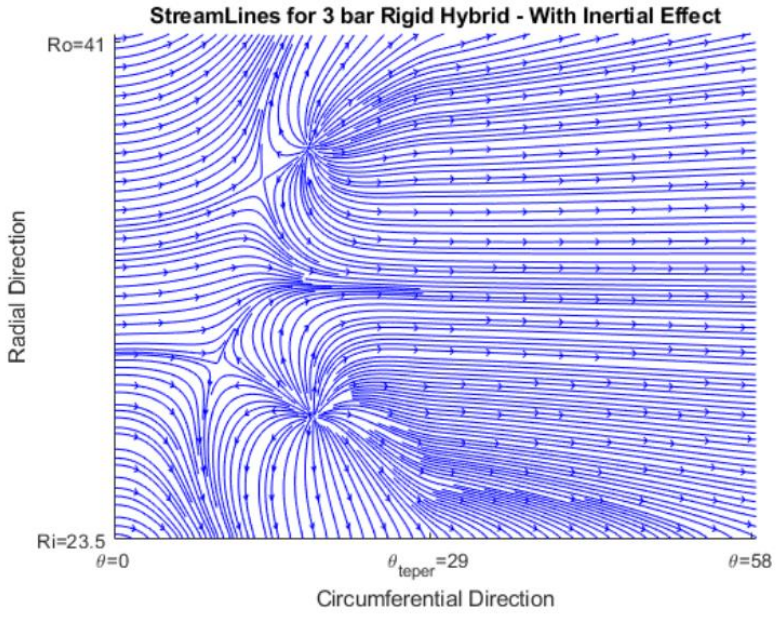

(b) Rigid Hybrid - Inertia

Figure 22: Rigid hybrid streamlines, P=3bar

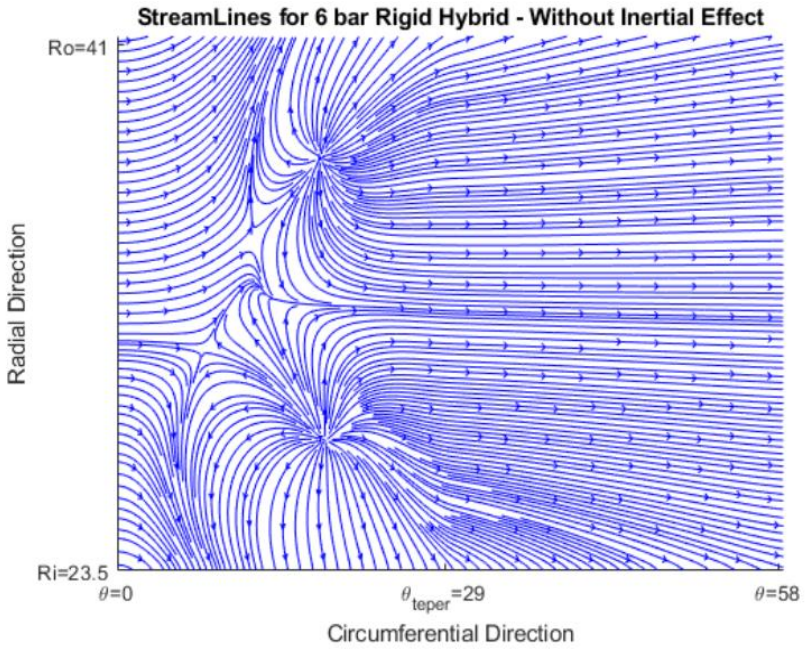

(a) Rigid Hybrid - No Inertia

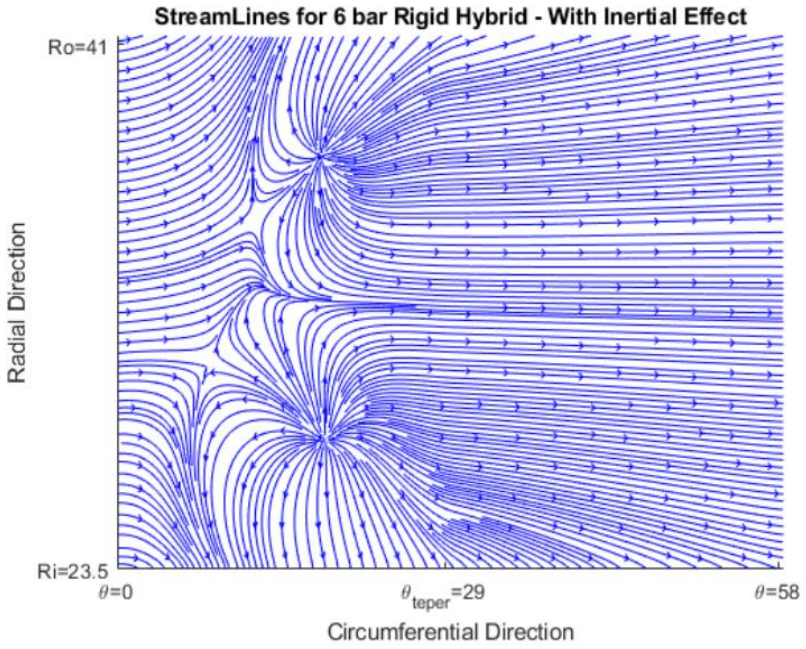

(b) Rigid Hybrid - Inertia

Figure 23: Rigid hybrid streamlines, P=6bar

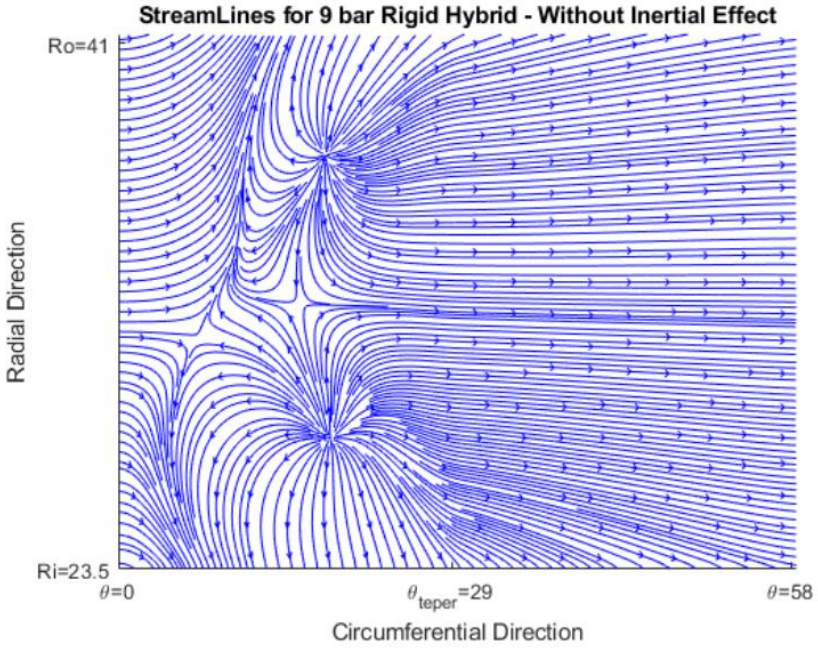

(a) Rigid Hybrid - No Inertia

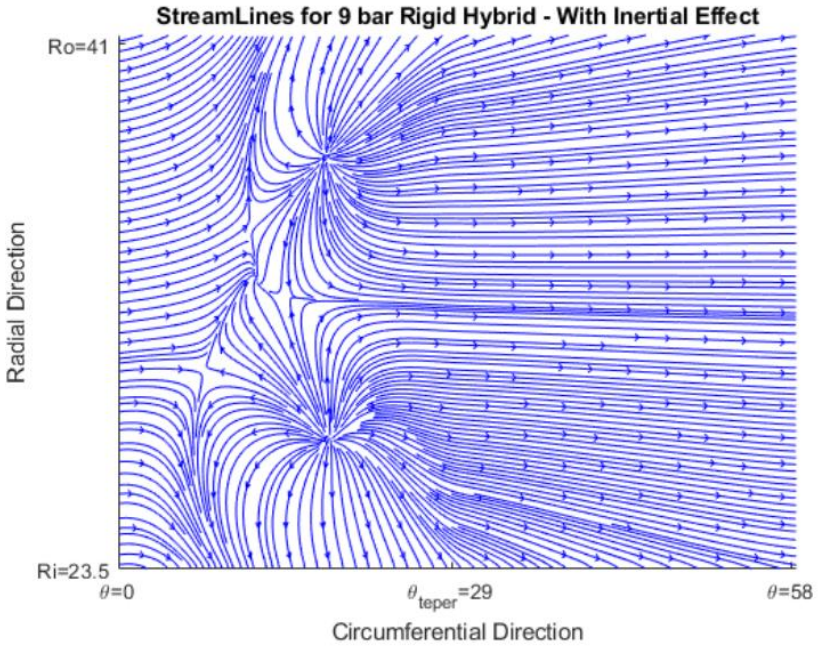

(b) Rigid Hybrid - Inertia

Figure 24: Rigid hybrid streamlines, P=9bar

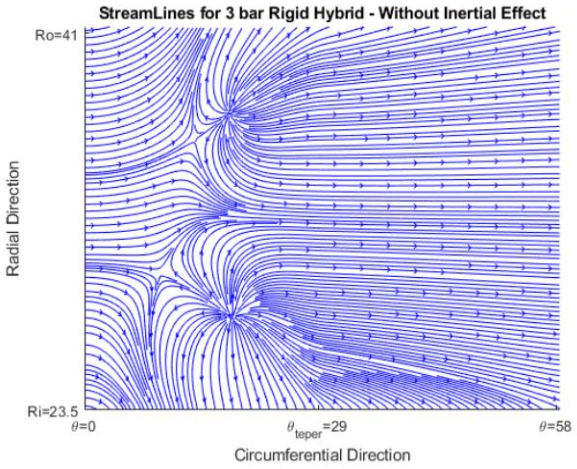

(a) Pb=3 bar

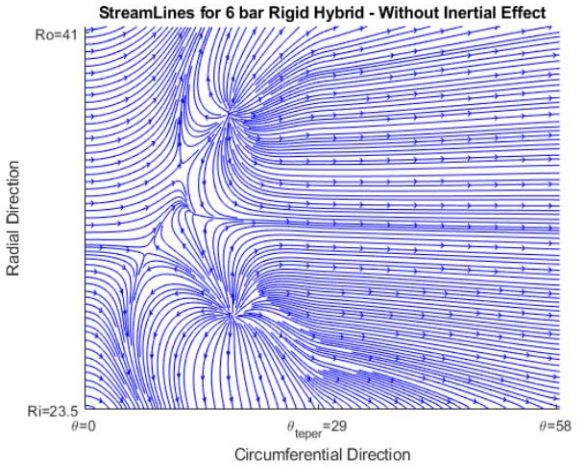

(b) Pb=6 bar

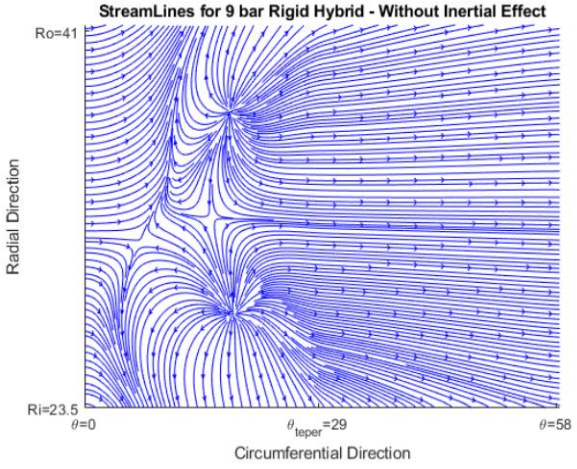

(c) Pb=9 bar

Figure 25: Rigid hybrid streamlines for all three cases – no Inertia

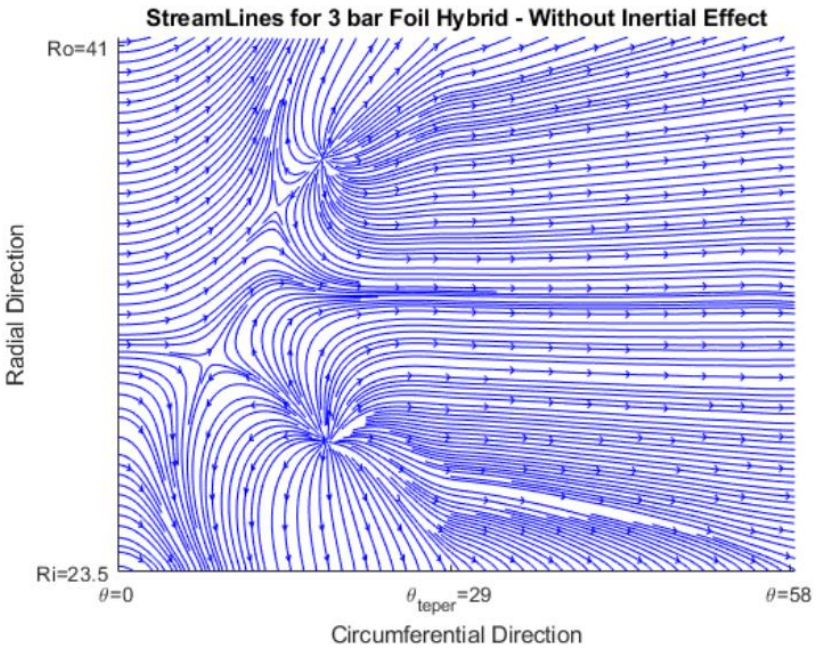

(a) Foil Hybrid - No Inertia

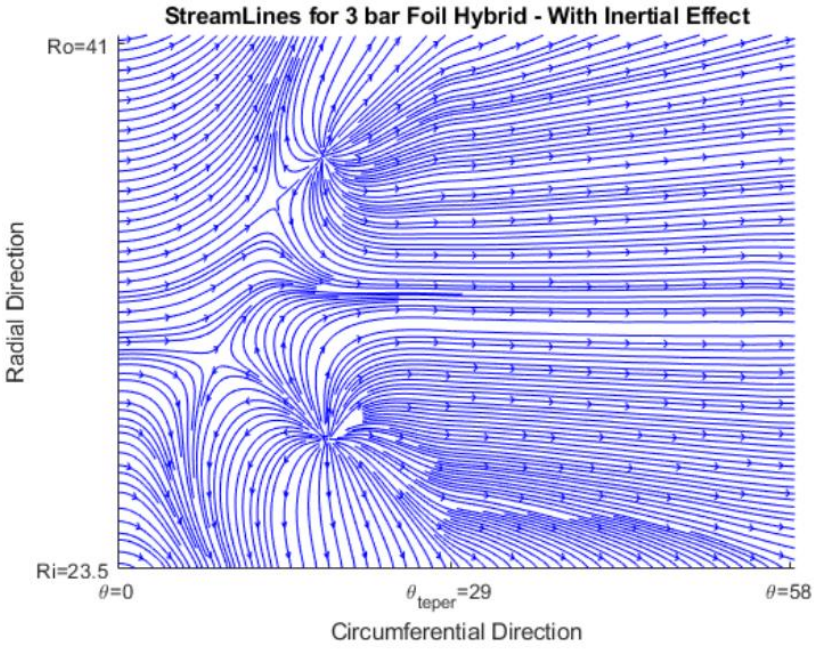

(b) Foil Hybrid - Inertia

Figure 26: Foil hybrid streamlines, P=3bar

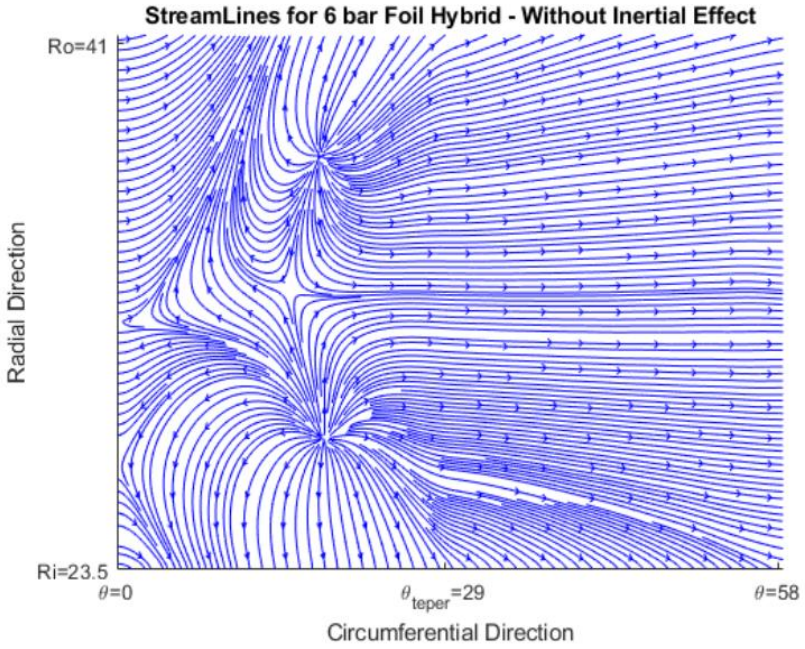

(a) Foil Hybrid - No Inertia

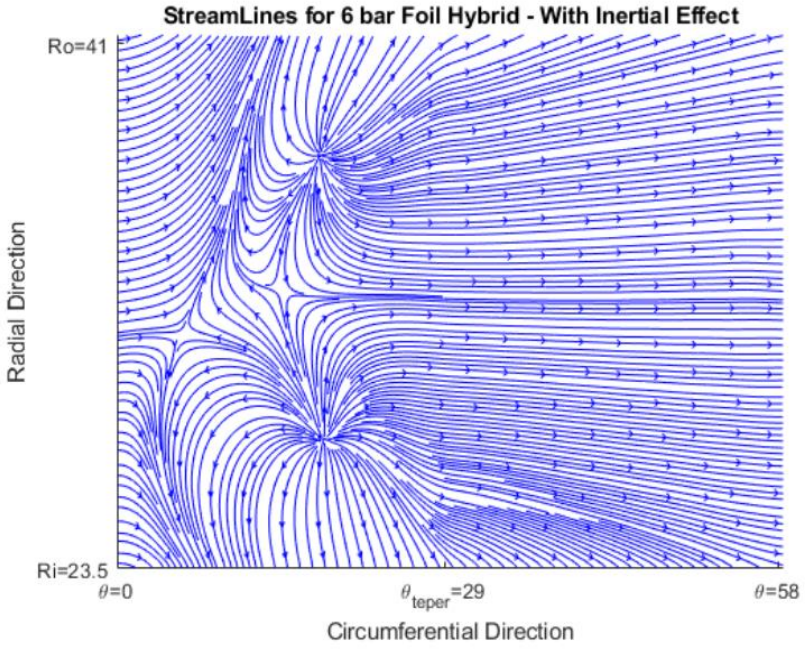

(b) Foil Hybrid - Inertia

Figure 27: Foil hybrid streamlines, P=6bar

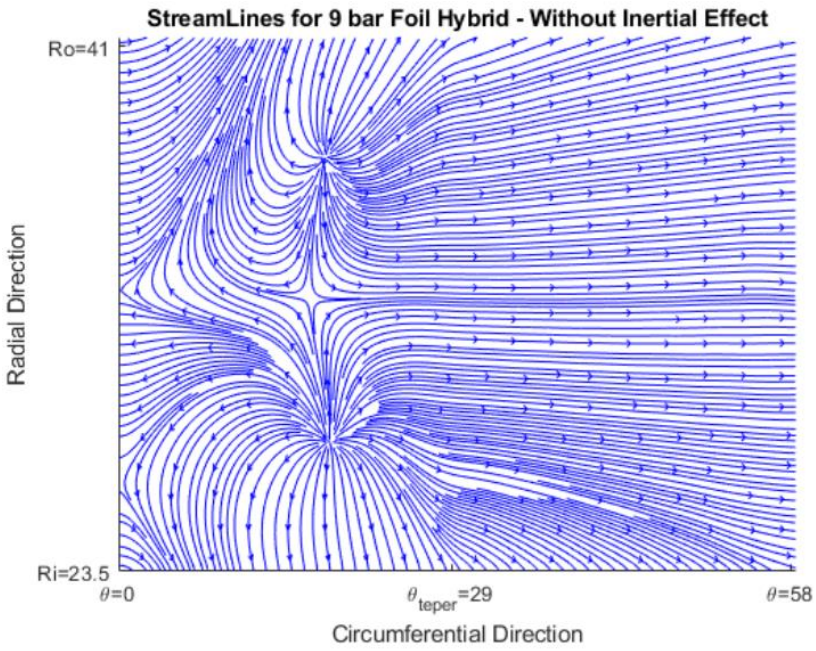

(a) Foil Hybrid - No Inertia

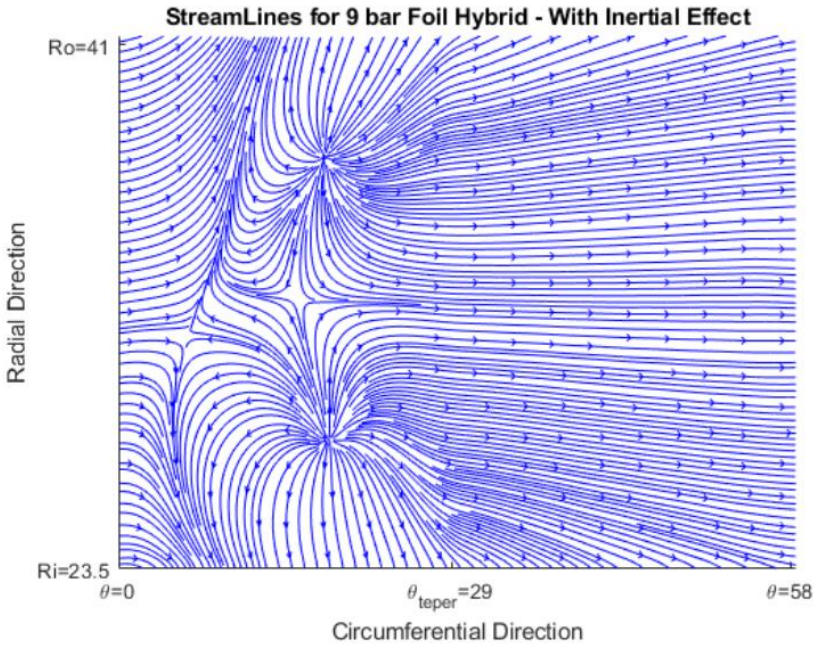

(b) Foil Hybrid - Inertia

Figure 28: Foil hybrid streamlines, P=9bar

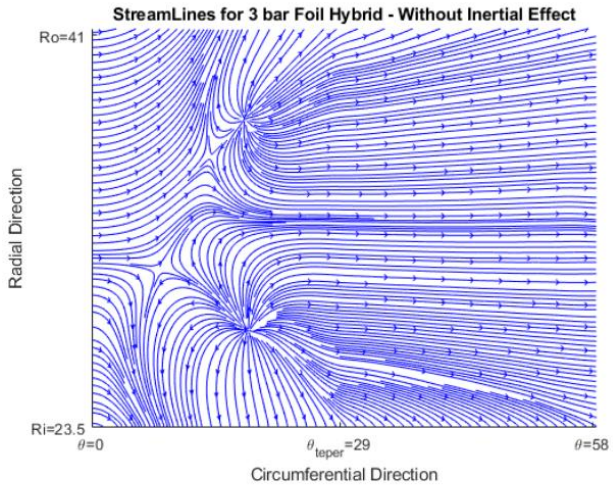

(a) Pb=3 bar

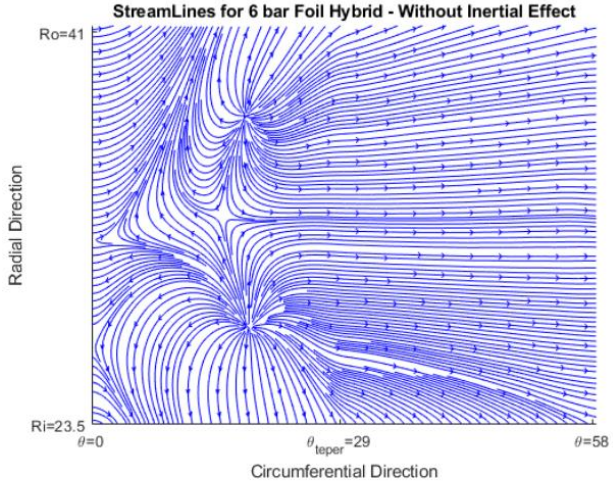

(b) Pb=6 bar

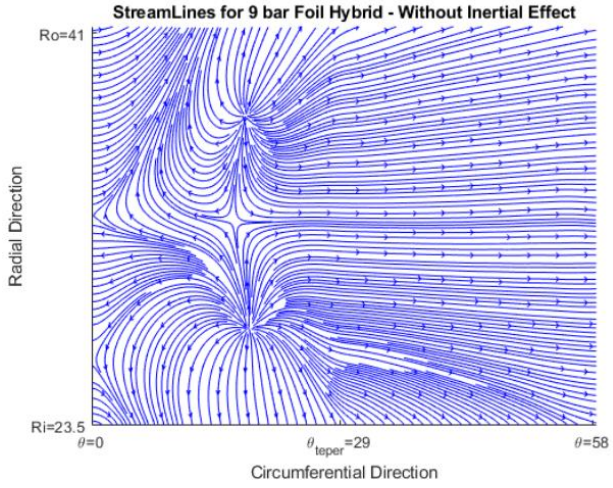

(c) Pb=9 bar

Figure 29: Foil hybrid streamlines for all three cases – no Inertia

Deflection

Another important thing that should be investigated when checking the foil bearing performance is the deflection of the bearing's bump foil, which provides the bearing's stiffness and damping coefficients. In this section, the foil deflection of the bearing when including and not including the inertia terms will be investigated it plays a major role in enhancing the bearing's load capacity is optimized to be stiffer, which may greatly help to decrease the leakage.

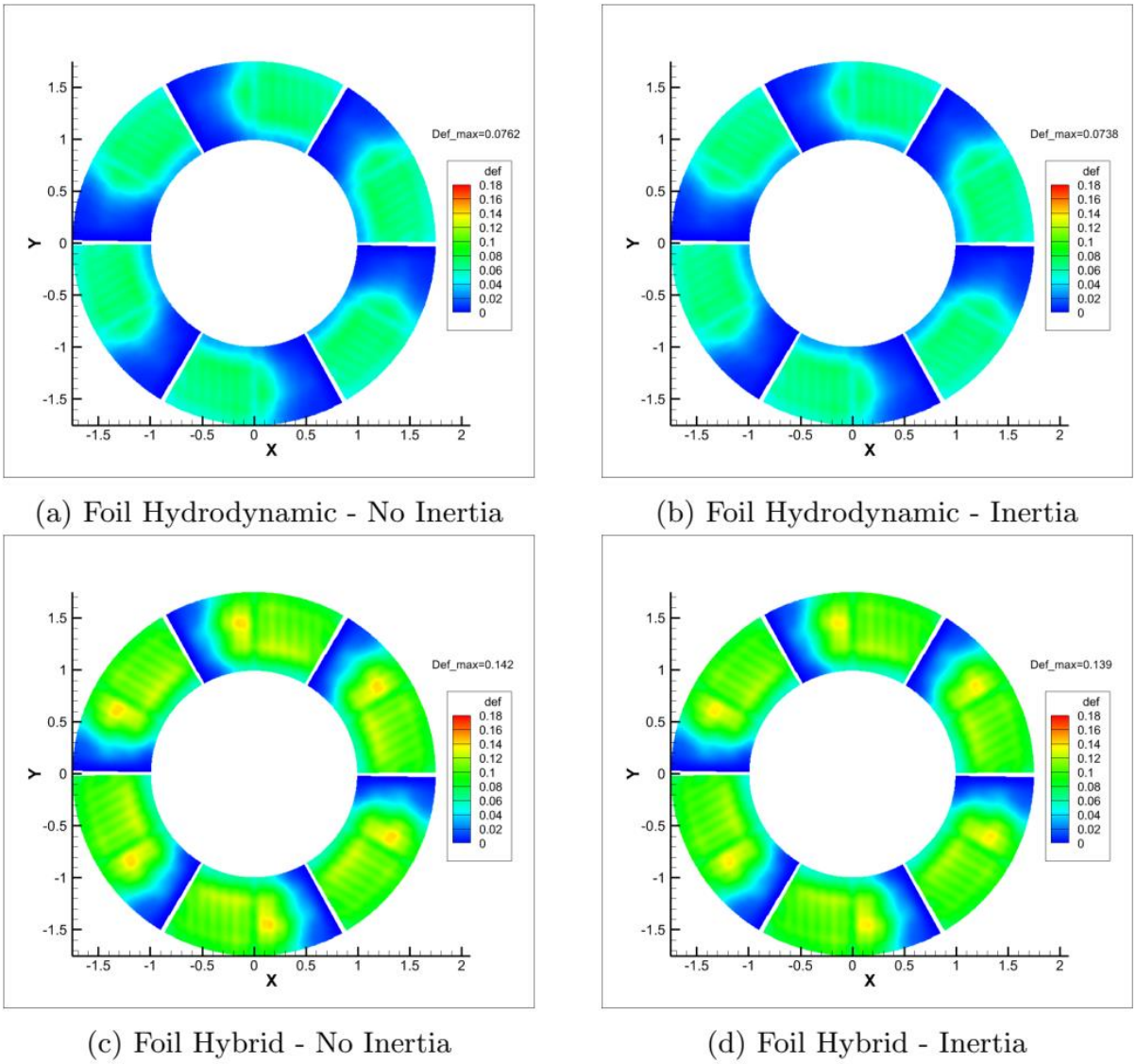

(a) Foil Hydrodynamic - No Inertia

(b) Foil Hydrodynamic - Inertia

(c) Foil Hybrid - No Inertia

(d) Foil Hybrid - Inertia

Figure 30: Nondimensional foil bearing's deflection, P=3bar

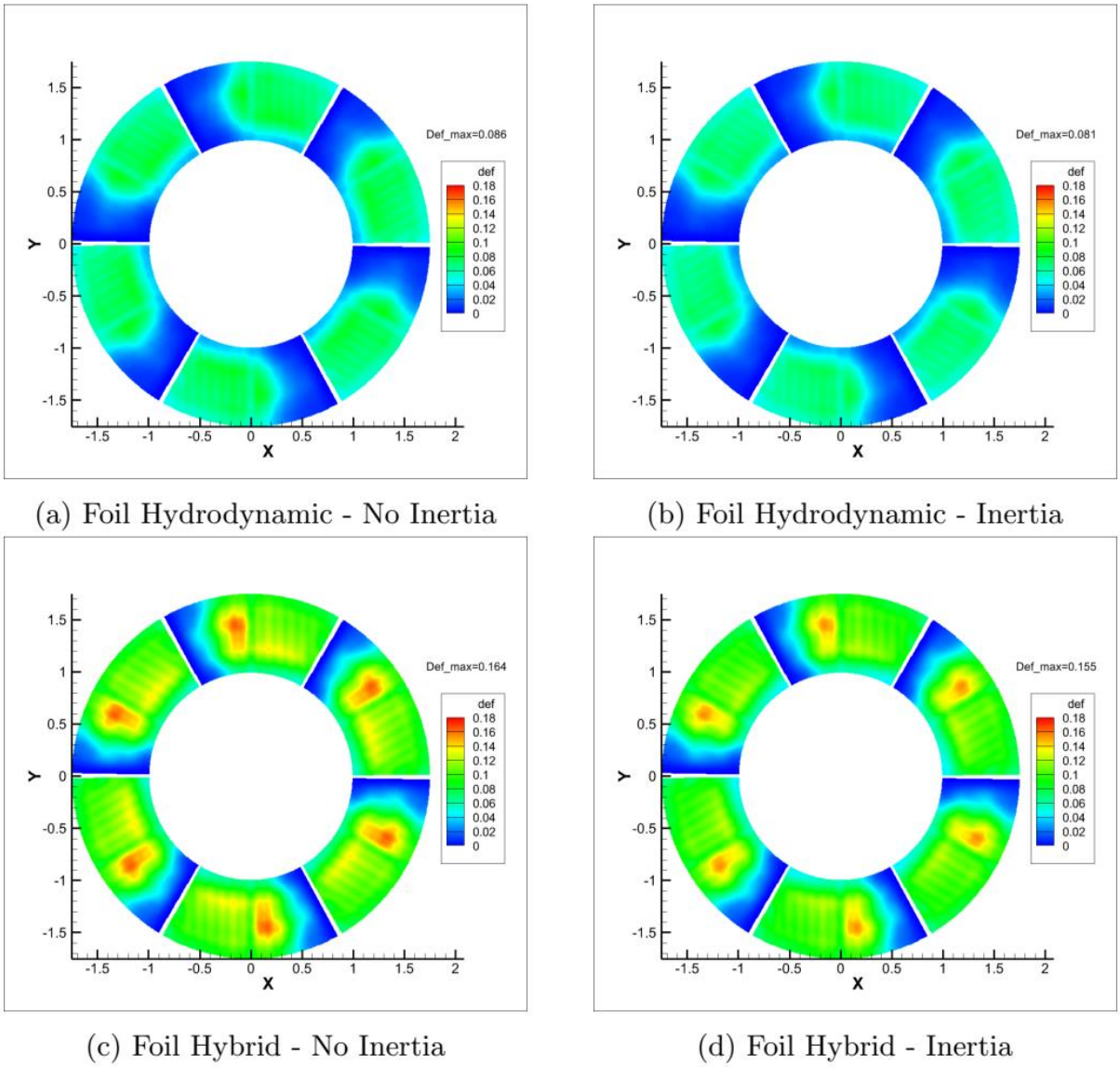

(a) Foil Hydrodynamic - No Inertia

(b) Foil Hydrodynamic - Inertia

(c) Foil Hybrid - No Inertia

(d) Foil Hybrid - Inertia

Figure 31: Nondimensional foil bearing's deflection, P=6bar

Figure 30, Figure 31, and Figure 32 illustrate the deflection happening in the bearing's top foil due to the increase in pressure. As explained in an earlier section that the pressure is higher for those cases when inertia terms are not included because the flow rate gets to be higher when including the inertia effect. Therefore, the leakage flow is mostly happening at the tapered region, where the maximum deflection occurs in the bearing. Furthermore, through these figures, it is possible to see

the maximum deflections that occur in both cases at different ambient pressures. Also, it is possible to see these numbers in Table 8 because it seems a bit hard to read them directly from the plots. These numbers get bigger as the pressure increases. In addition, the gap between the two maximum numbers for both cases while including and not including the inertia terms gets larger as the pressure increases.

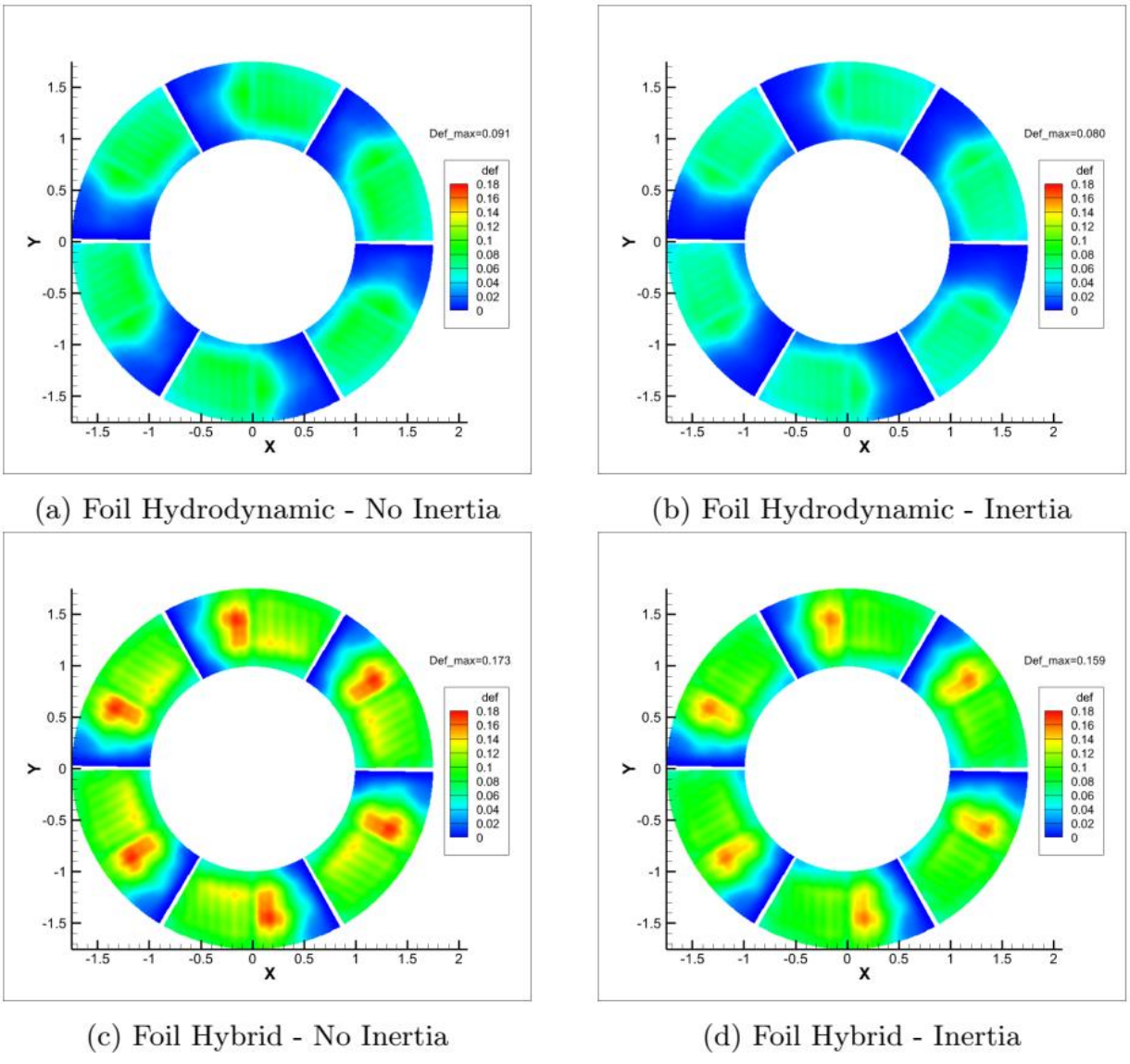

(a) Foil Hydrodynamic - No Inertia

(b) Foil Hydrodynamic - Inertia

(c) Foil Hybrid - No Inertia

(d) Foil Hybrid - Inertia

Figure 32: Nondimensional foil bearing's deflection, P=9bar

Table 8: Maximum deflections of both cases with including and without including the inertia terms

-	Foil Hydrodynamic		Foil Hybrid	
Pressure (bar)	Without Inertia	With Inertia	Without Inertia	With Inertia
3	0.076	0.074	0.142	0.139
6	0.086	0.081	0.164	0.155
9	0.091	0.080	0.173	0.159

Bearing's Load Capacity

This section discusses the main objective of this research, which is the bearing's load capacity. Generally, the bearing's load capacity is the core aspect to be investigated when designing and testing the bearings' performance. It is an important matter because it indicates how much load can the bearing take while operating. Therefore, it is crucial as it can attenuate the bearing's ability to operate flexibly while exerting a higher load. As has been discussed in the pressure section that the inertia terms added to the classic Reynolds lubrication equation play a major role in reducing the pressure profile of the bearing. Therefore, that, in turn, will heavily reduce the bearing's load capacity as illustrated in the next figures. Figure 33, Figure 34, Figure 35, and Figure 36 illustrate the bearing's load capacity versus the pressure for the rigid hydrodynamic, rigid hybrid, foil hydrodynamic, and foil hybrid, respectively. Figure 33 shows the load capacity for both cases of including and not including the inertia terms, where both load capacities are almost the same and they tend to differ as the pressure increases beyond 3 bar, but it seems to be 4 bar in the case of the rigid hybrid as illustrated in Figure 34. However, that seems to be exactly at 2 bar for both cases of foil bearing as shown in Figure 35 and Figure 36. The load capacity when the inertia effect is included tends to decrease as the pressure increases for all four cases. However, it seems to be a bit less in the case of rigid bearings because there is no deflection, and the load capacity tends to decrease a bit more in the case of the rigid hydrodynamic bearing since there is

no hydrostatic air supplying the system. However, for both cases of foil bearing, the load capacity drops further to a greater amount due to the deflection.

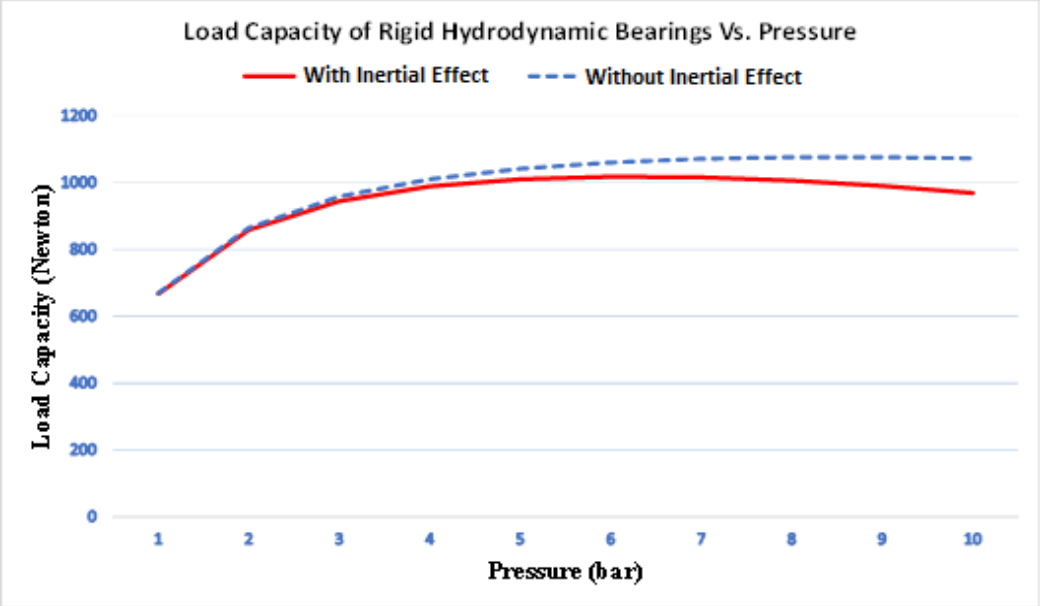

Figure 33:Load capacity Vs pressure of rigid hydrodynamic

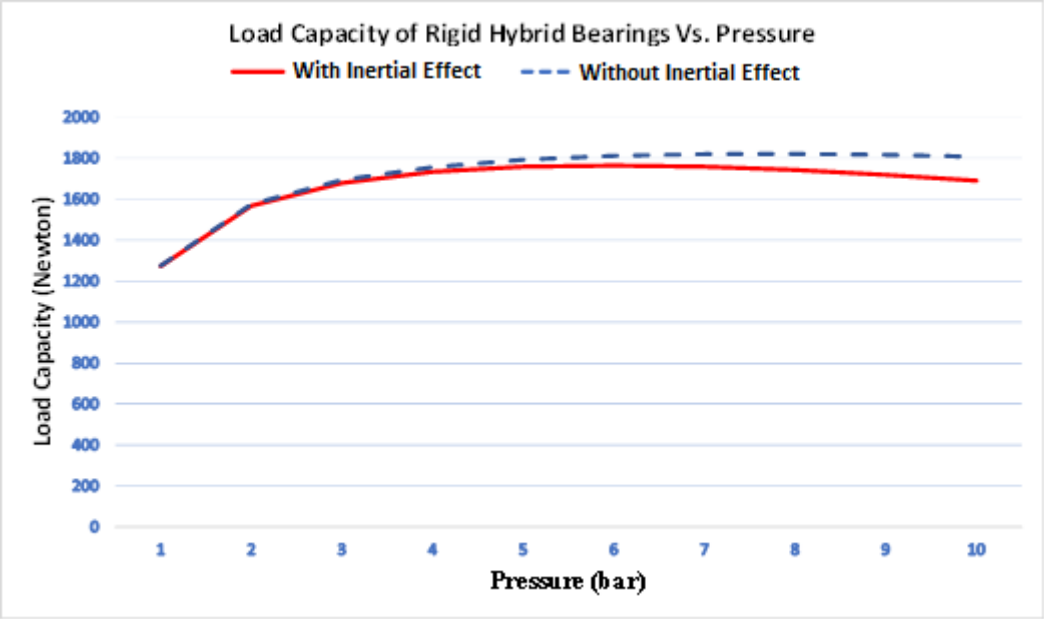

Figure 34: Load capacity Vs pressure of rigid hybrid

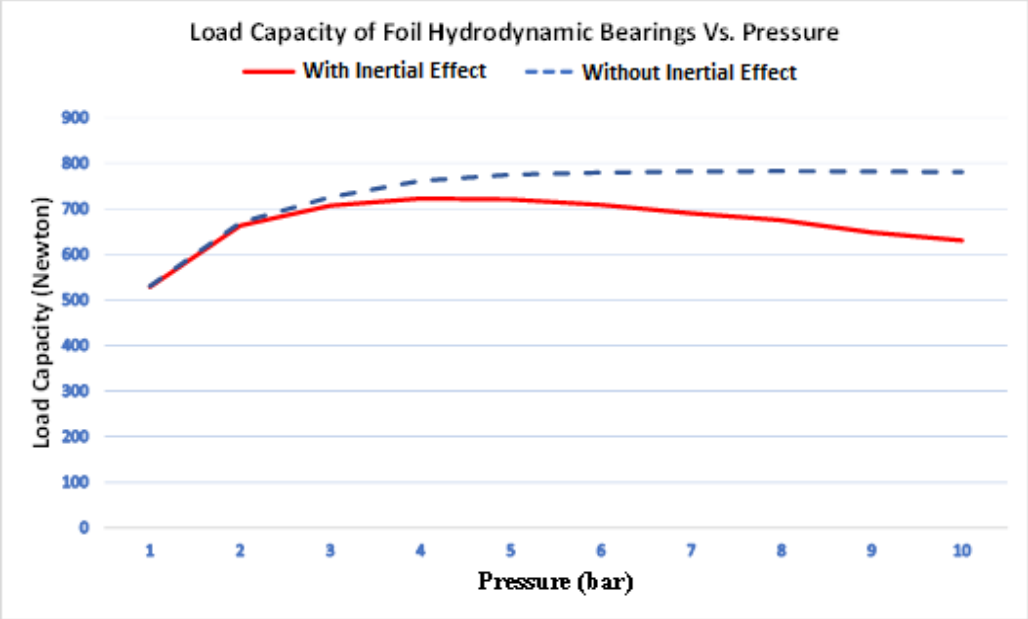

Figure 35: Load capacity Vs pressure of foil hydrodynamic

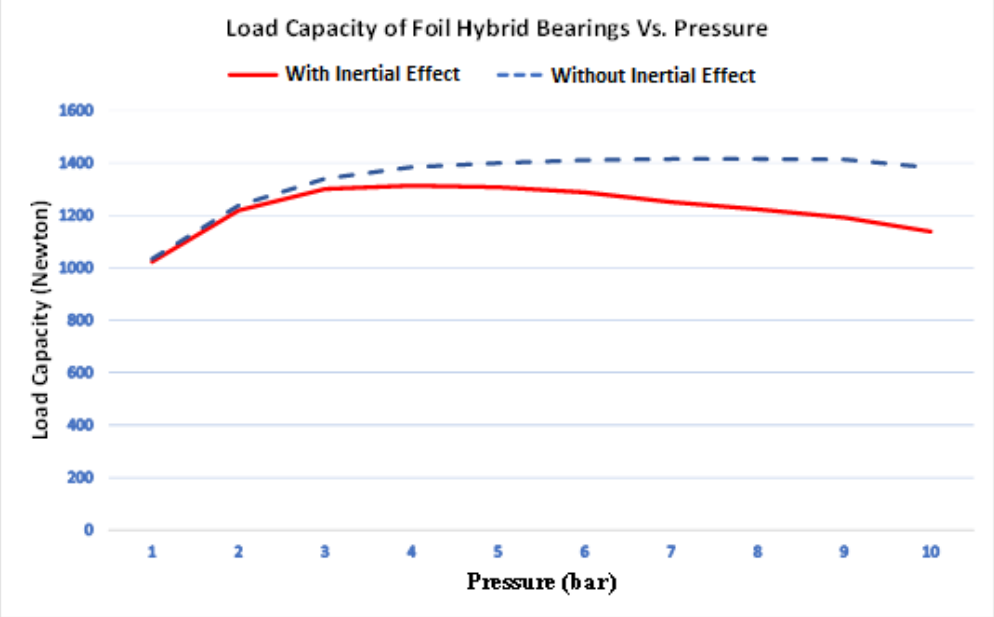

Figure 36: Load capacity Vs pressure of foil hybrid

Chapter 6: CONCLUSION

Both rigid and foil gas thrust bearings are widely used bearings in turbomachine applications. The thrust bearing is used to prevent the movement of the shaft along its length. The thrust bearing can operate in either hydrodynamic or hybrid mode. When dealing with viscous lubricants, such as oil, inertia terms can be neglected since the viscous force dominates. However, when dealing with water or denser gases, the inertia effect should be considered. The classical Reynolds equation should be modified to consider those terms. The inertia effect most of the time is linked to the turbulent flow; however, the inertia effect also appears when the flow is laminar. Inertia terms can always be considered when the system operates at very high speed and undergoes very high loading, where the centrifugal force has a negative influence in attenuating the bearing's load capacity. According to many former literatures, the convective effect and centrifugal effect can be decomposed to be analyzed separately because the convective effect has a positive influence while the centrifugal effect has a negative influence. The gas thrust bearing loses a great deal of its load capacity as the ambient pressure increases due to the leakage flow that is mostly happening at the tapered region, but it appears to be greater to some extent in the case of the foil bearing, where the maximum deflection of the bump foil occurs at the tapered region.

REFERENCES

[1] Dykas, B., Bruckner, R., Christopher, D., Brian, E., Prahl, J., 1999, "Design, Fabrication, and Performance of Foil Gas Thrust Bearings for Microturbomachinery Applications"

[2] Song, Z., Guoa, F., Liua, Y., Liua, X., Wang, Y.,2016, "Inertia Effect on the Load Capacity of Large Water-Lubricated Thrust Bearing"

[3] Hashimoto, H., 1989, "The Effects of Fluid Inertia Forces on the Static Characteristics of Sector-Shaped, High-Speed Thrust Bearings in Turbulent Flow Regime"

[4] Los Alamos National Laboratory, 1943, "Periodic Table of Elements: LANL, " https://periodic.lanl.gov/index.shtml

[5] Briggs, M., Prahl, J., Bruckner, R., Dykas, B.,2008, "High Pressure Performance of Foil Journal Bearings in Various Gases"

[6] Belforte, G., Raparelli, T., Viktotov, V., 1999, "Theoretical investigation of Fluid Inertia Effects and Stability of Self-Acting Gas Journal Bearings"

[7] Kakoty, S. k., Majumdar, B.C., 2000, "Effect of Fluid Inertia on Stability of Oil Journal Bearings"

[8] Pinkus, O., and Lund J., 1981, "Centrifugal Effects in Thrust Bearings and seals under Lamina Conditions"

[9] Khonsari, M., and Booser, E., 2017, "Applied Tribology: Bearing Design and Lubrication," John Wiley & Sons, Chichester, UK, pp. 189, Chapter 6.

[10] Patankar, S., 1980, "Heat Transfer and Fluid Flow," Hemisphere Publishing Corporation, USA, Chapter 3.

[11] Anderson, J., 2017 "Fundamental of Aerodynamics," Published by McGraw-Hill Education, USA, Chapter 1.

[12] Cengel, Y., and Cimbala, J., 2006, "Fluid Mechanics: Fundamentals and Applications," McGraw-Hill Companies, New York, NY, pp. 324, Chapter 8.

[13] Supercritical Co_2 Tech Team, n.d., "Clean Coal & Natural Gas Power Systems, " https://www.energy.gov/supercritical-co2-tech-team

[14] Nguyen LaTray, and Daejong Kim, 2021, "Novel Thrust Foil Bearing With Pocket Grooves for Enhanced Static Performance."